Effect of surfactant addition and viscosity of the continuous phase on flow fields and kinetics of drop formation in a flow-focusing microfluidic device

Kiratzis, Ioannis; Kovalchuk, Nina M.; Simmons, Mark J.h.; Vigolo, Daniele

[Link to publication on Research at Birmingham portal](#)

Effect of surfactant addition and viscosity of the continuous phase on flow fields and kinetics of drop formation in a flow-focusing microfluidic device.

Ioannis Kiratzis[a], Nina M. Kovalchuk[a], Mark J. H. Simmons[a,*], Daniele Vigolo[a,b,c*]

[a] *School of Chemical Engineering, University of Birmingham, Edgbaston, Birmingham B15 2TT, UK*

[b] *School of Biomedical Engineering, University of Sydney, Sydney, NSW 2006, Australia*

[c] *The University of Sydney Nano Institute, University of Sydney, Sydney, NSW 2006, Australia*

* corresponding authors: daniele.vigolo@sydney.edu.au, M.J.Simmons@bham.ac.uk

Abstract

Droplet formation in a flow focusing microfluidic device was studied for capillary numbers between 10^{-4} and 10^{-1}. The addition of a cationic surfactant to the dispersed phase and the effect of the continuous phase viscosity on droplet size, neck kinetics and flow fields inside the drop was investigated. Droplet size decreased with an increase of the capillary number following a power law with an exponent dependent on drop confinement. At 1-3 ms before pinch-off, the neck thinning rate is dependent on surfactant concentration and increases closer to pinch-off. For the 96 mPa·s continuous phase, the two-fluid Stokes regime is observed with an effective interfacial tension smaller than the equilibrium value, suggesting a negative contribution of Marangoni stresses. During necking, velocities along the neck interface for the surfactant laden cases are smaller due to Marangoni phenomena. During expansion, increased fluid velocities and recirculation are observed.

Keywords: Microfluidics, Ghost Particle Velocimetry, Droplet formation, Surfactants, Marangoni phenomena

1. Introduction

Microfluidic methods allow for the precise production and manipulation of micrometre-sized droplets (Anna, 2016), with applications including cell encapsulation (Qin et al., 2020), biological macromolecules characterisation (Ferreira et al., 2018), DNA studies (Pellegrino et al., 2018) as well as cell and protein studies (Ven et al., 2018). The small length scales associated with microfluidic devices result in laminar flow fields, while the increased surface-to-volume ratio and small timescales involved mean that the interfacial dynamics are highly important (Bruus, 2007).

The flow rates of the dispersed and continuous phase as well as the geometry of the microfluidic device determine the flow field which is responsible for the deformation of the interface and ultimately the droplet formation. In most droplet formation microfluidics experiments, droplet monodispersity is above 97% (Umbanhowar et al., 2000) with the most common junction configurations used being co-flow, cross—flow (T-junctions) and flow focusing (Anna, 2016).

A common co-flow design employs a tapered capillary which is used to introduce the dispersed phase into the co-flowing continuous phase, forming a stream of droplets (Wu et al., 2017). Droplets grow at the tip of the capillary and detach when they reach a critical size where the drag of the continuous phase surpasses interfacial tension forces.

Cross-flow microfluidic droplet formation was first implemented using a T-shaped microfluidic device by (Thorsen et al., 2001); a later study reported that the size of the droplets was dependent upon the flow rates of both the dispersed and continuous phases (Nisisako et al., 2002, Glawdel et al., 2012, Anna, 2016).

For flow focusing geometries three characteristic regimes can be identified (Cubaud and Mason, 2008), namely threading (Figure 1a), where a stable thread of the dispersed phase is

formed, jetting (Figure 1b), where the dispersed phase forms a thread which breaks into drops after some distance from the junction and dripping (Figure 1 c), where droplets are formed at the junction. In the dripping regime, of interest for this study, the droplet formation process is a competition between the interfacial tension force that acts against droplet break-up and the drag force of the continuous phase that pulls the droplet downstream Interfacial tension force can be estimated as (Bhunia et al., 1998)

$$F_\sigma = \gamma P \tag{1}$$

where γ is interfacial tension, and P_N is the neck perimeter. The maximum neck perimeter can be approximated as the chanel perimeter. The drag force can be estimated as

$$F_D \sim \pi \mu_c \frac{2n+3}{n+1} D_d (u_c - u_d) \tag{2}$$

where μ_c is the continuous phase viscosity (Pa·s), n is the viscosity ratio, D_d is the droplet diameter and u_c - u_d (m s^{-1}) is the relative velocity between the continuous phase and the droplet velocity (Husny and Cooper-White, 2006). Dripping can de divided into three stages (Figure 1 d), expansion, necking and pinch-off. After the pinch-off of the previous droplet, the dispersed phase retracts slightly into the dispersed phase channel due to interfacial tension and then it moves again towards the main channel. In the first stage, referred to as ***expansion***, the dispersed phase invades the junction and expands into the main channel. In some cases, the expanding drop completely blocks the flow of the side channels. As the pressure in the side channels increases further, the expanding drop starts growing mainly in the axial direction towards the main channel, forming a liquid bridge connecting the expanding droplet to the bulk of the dispersed phase. The start of the ***necking*** stage occurs when the curvature along the interface of the bridge becomes negative; the thinnest part of the bridge is defined as the neck. As the necking stage progresses the neck becomes thinner as the bridge buckles under the flow of the continuous phase. Moreover, with the neck diameter decrease, the capillary pressure

inside it becomes larger than that in the drop, accelerating the neck's liquid expulsion. Eventually, the neck ruptures in what is defined as the ***pinch-off*** stage.
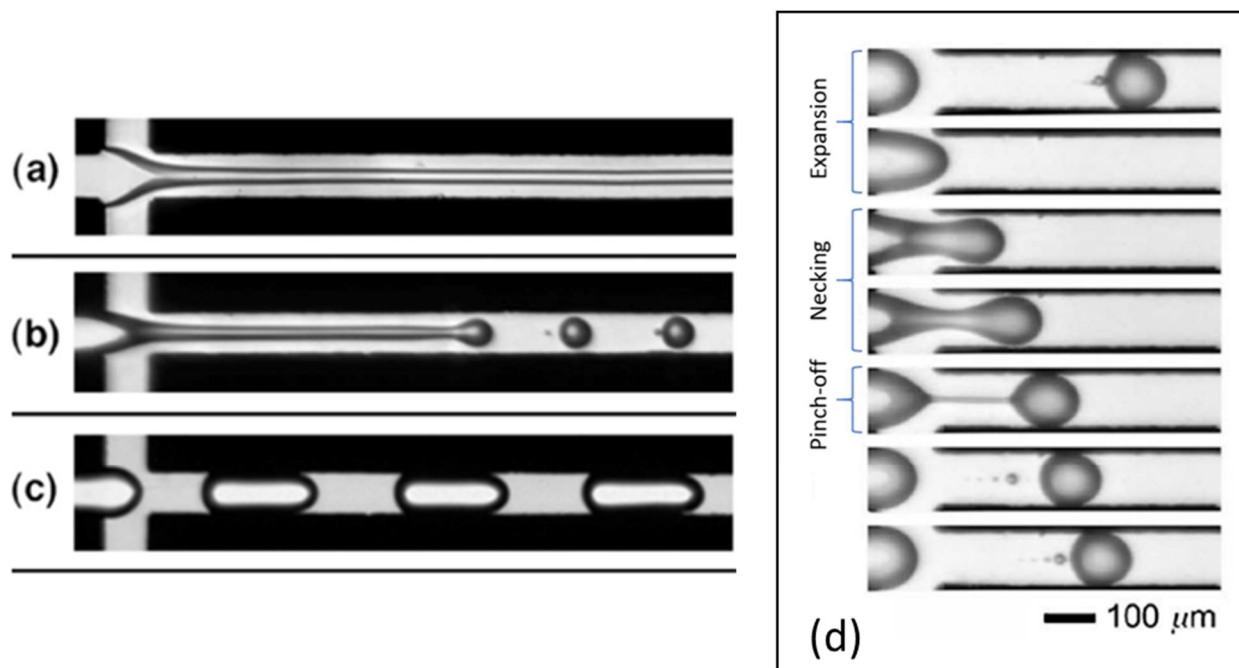
Figure 1 Flow regimes in a cross flow microfluidic device. a: threading, b: jetting, c: dripping and d: droplet formation under dripping. Images adapted from (Cubaud and Mason, 2008). Copywrite 2008 with permission for AIP.

Surfactants are omnipresent in emulsification processes, regardless of the equipment used. In microfluidics, the addition of surfactant results in the lowering of interfacial tension, which facilitates droplet break-up; it enables control of the wetting conditions on the channel walls and prevents droplet or bubble coalescence. Surfactant molecules can be transported to/from and at the interface through diffusion and convective flows, including Marangoni convection triggered by non-uniform surfactant distribution over the interface. The processes of surfactant transfer have their own individual time scales, which compete with the droplet formation time scales. This might lead to the development of interfacial tension gradients, especially at intermediate surfactant concentrations (Wang et al., 2009). In particular, the diffusive transport of surfactant to the interface is often much slower than the microfluidic droplet formation process (Diamant and Andelman, 1996) and is controlled by the diffusion coefficient and concentration of the surfactant. Furthermore, redistribution of surfactant occurs due to

convective mixing. These flows establish a boundary layer close to the interface, which determines the length over which surfactant molecules need to diffuse through to migrate to the interface (Alvarez et al., 2012). The thickness of this layer decreases with an increase of Peclet number defined as

$$Pe = \frac{Lu}{D} \qquad (3)$$

Where L is a characteristic length, u is the fluid velocity and D is the diffusion coefficient Lastly, Marangoni phenomena redistribute surfactant along the interface and are proportional to the interfacial tension gradient and depend on the viscosity of both liquid phases (Nowak et al., 2017).

Given the interplay of these phenomena, although the size of droplets decreases in the presence of surfactant (Anna, 2016), the actual value of interfacial tension during drop formation can be far from equilibrium (Cui et al., 2020, Kovalchuk et al., 2016). It was observed that the produced droplet sizes are larger in the cases where the surfactant transport dynamics are slow and surfactant depletion phenomena can arise (Xu et al., 2012). An experimental study on the kinetics of thinning of liquid bridges has shown that they are affected by surfactant dynamics when a surfactant with a low critical micelle concentration (cmc) value is used. In contrast, for a surfactant with a cmc $\geq$ 15 mM, the kinetics are determined by the equilibrium interfacial tension (Kovalchuk et al., 2016). According to (de Saint Vincent et al., 2012) the interfacial tension at the neck increases close to pinch-off, indicating depletion of surfactant in that region. Microfluidics has been used to estimate short-time dynamic interfacial tension of surfactant solutions, for example, by analysis of the changes of the droplet surface area in a T-junction (Glawdel and Ren, 2012) and by measuring the droplet size or shape (Xu et al., 2008, Brosseau et al., 2014).

A general description of surfactant behaviour is far from being complete. Flow visualisation provides an opportunity to better understand surfactant mass transport. Planar Laser Induced Fluorescence (PLIF) has been used to describe the spatiotemporal distribution of a fluorescent surfactant (Dong et al., 2019) and micro Particle Image Velocimetry (μ-PIV) has shown changes in droplet flow patterns in the presence of surfactant, attributed to the presence of Marangoni stresses on the interface of the expanding droplet (Roumpea et al., 2019). Furthermore, studies on drop coalescence with a flat liquid/liquid interface showed that the spatiotemporal distribution of surfactant affects the coalescence process by inducing partial or total coalescence (Chinaud et al., 2016).

The recently developed Ghost Particle Velocimetry (GPV) (Buzzaccaro et al., 2013, Riccomi et al., 2018) technique affords this topic further examination, as the nano-sized tracers used enable velocimetric analysis of high-speed small-scale phenomena occurring in emulsification (Pirbodaghi et al., 2015).

This paper presents the results of an experimental study that uses high-speed videography and GPV to improve understanding of the physics of surfactant mass transport during droplet formation as a function of surfactant concentration and continuous phase viscosity. Two different cationic surfactants are used, $C_{10}TAB$ and $C_{12}TAB$. At any chosen equilibrium interfacial tension, these two surfactants differ in their adsorption kinetics due to difference in corresponding concentration values including values of cmc. The dependence of flow rate and viscosity of the continuous phase, surfactant type and concentration upon the droplet size is investigated, followed by a study of the kinetics of neck thinning examining the effect of surfactant for instances close and away from the pinch-off. Finally, an improved hydrodynamic profile for the expansion and necking stage is extracted using GPV and the

observed hydrodynamics are linked with the dynamic surfactant effects during droplet formation.

2. Materials and experimental methods

2.1. Materials

The physical properties of the studied liquids are presented in

Table 1. Silicone oils with various viscosities (4.6, 19, 96 mPa·s, Merck) and a refractive index of 1.403 were used as the continuous phase. The dispersed phase was an aqueous solution of glycerol (purity > 99%, Merck), 52% by weight in double distilled water, produced by a water still (Aquatron A 4000D, Stuart), giving the same refractive index as the silicone oils (Pala Rosas et al., 2017). The matched refractive index between both phases allows close observation of the interfaces in GPV studies.

Table 1 Physical properties of the fluids involved. a: (Cheng, 2008), b: (Roumpea et al., 2019), c: supplier data sheet (Merck)

	Density (kg m^{-3})	Dynamic viscosity (mPa·s)	Interfacial tension (mN·m^{-1})
52% Glycerol- water	1133[a]	6[b]	
5 cSt silicone oil	913[c]	4.6[c]	32
20 cSt silicone oil	950[c]	19[c]	32
100 cSt silicone oil	960[c]	96[c]	32

The surfactants, $C_{10}TAB$ and $C_{12}TAB$ (both with purity > 98%, Merck), were used without additional purification. 1 g·L^{-1} of Methyl violet dye (Merck) was added to the aqueous phase to produce a large enough contrast for optical observation (Nowak et al., 2017). 0.2% by volume of a dispersion of polystyrene nanoparticles of 200 nm (10% by weight, Merck) were

dispersed in the aqueous phase for the GPV experiments (Riccomi et al., 2018, Martino et al., 2016, Schofield et al., 2020). Figure 2 displays the equilibrium interfacial tensions of the solutions used in this study, measured using a SINTERFACE PAT1P optical tensiometer. The cmc of $C_{12}TAB$ in a 52% by weight glycerol solution found from Figure 2 is 21 mM in agreement with literature (Roumpea et al., 2019) and the cmc of $C_{10}TAB$ is 76 mM. The equilibrium interfacial tension values for $C_{12}TAB$ solutions with the same glycerol content in a 4.6 mPa·s continuous phase can be found in literature (Kovalchuk et al., 2018b). It is clear from Figure 2 that the interfacial tension is practically independent of silicone oil viscosity. This result was expected, considering that the interfacial tensions for surfactant-free glycerol/water mixture in contact with three studied silicone oils are similar.
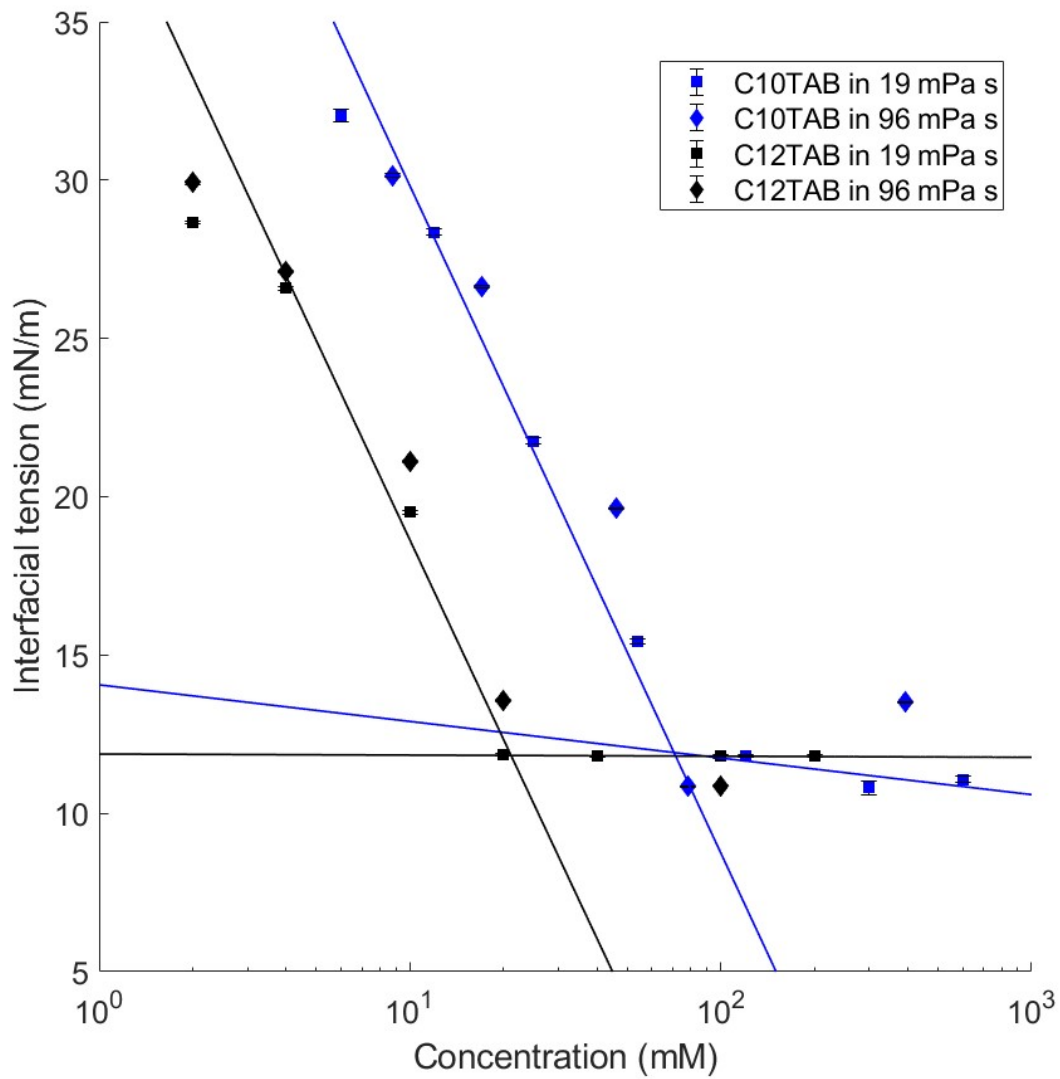
Figure 2 Equilibrium interfacial tensions for the solutions used in the study

The data presented in Figure 2 were fitted to Szyszkowski–Langmuir equation

$$\gamma - \gamma_0 = RT\Gamma_\infty \ln(1 + bc) \qquad (4)$$

using IsoFit free software (Aksenenko, 2001, Aksenenko, 2021). γ_0 and γ are the interfacial tensions of the surfactant-free and the surfactant-laden system respectively, and R and T are the ideal gas constant and the absolute temperature. The adsorption isotherm of the Langmuir model is

$$\Gamma = \Gamma_\infty \frac{bc}{1+bc} \tag{5}$$

where Γ is the surfactant adsorption, Γ_∞ is the limiting adsorption, b is the adsorption constant and c is the surfactant bulk concentration (data shown in Table 2). For each surfactant the isotherm data from the different continuous phases is combined since there is minimal effect of viscosity. The calculated values in Table 2 are in good agreement with data for the same surfactants at water-air interfaces (Mucic et al., 2011) and with data for $C_{10}TAB$ in water in contact with 50 cSt silicone oil (Kovalchuk et al., 2019).

Table 2 Limiting adsorption and adsorption constants for the surfactants used in the study. The values in the parenthesis are the literature values. a:(Kovalchuk et al., 2019) . b: (Mucic et al., 2011)

	$C_{10}TAB$	$C_{12}TAB$
Γ_∞ (mol m^{-2})	$1.4 \cdot 10^{-5}$ $(9.1 \times 10^{-6})^a$	$1 \cdot 10^{-5}$ $(1.12 \times 10^{-5})^b$
b (m^3 mol^{-1})	$9 \cdot 10^{-3}$ $(2.6 \times 10^{-2})^a$	$6 \cdot 10^{-2}$ $(1.61 \times 10^{-1})^b$

2.2. Microfluidic system

A flow-focusing microfluidic device is used to produce water-in-oil droplets in the dripping regime under various flow rate conditions. Figure 3a displays the experimental set-up while Figure 3b a snapshot, along with the dimensions, of the microfluidic device used. The depth of the channels (not shown) is 150 μm. A silicon mould was fabricated by photolithography as described in (Xia and Whitesides, 1998). The microfluidic device was then created by standard soft-lithography, using polydimethysiloxane PDMS (Sylgard 184, Dow Corning). PDMS is mixed with the curing agent (10:1 by weight), poured into the mould, degassed in a vacuum chamber and cured in an oven at 70 ºC for 90 mins.
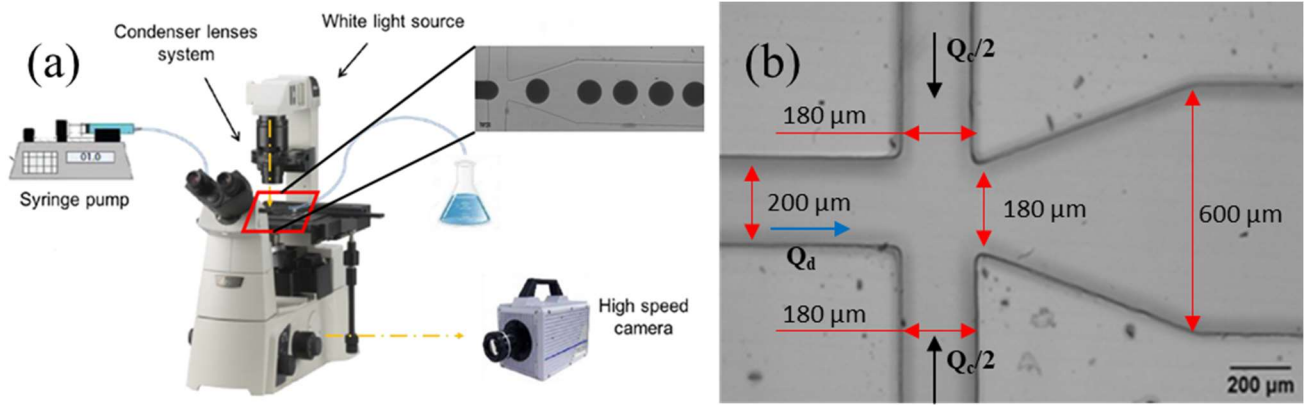
Figure 3 a: Schematic of the experimental set-up. b: Snapshot of the microfluidic device. Q_d and Q_c refer to the dispersed and continuous phase flow rates respectively along with the flow directions

For the droplet formation experiments, two syringe pumps (AL-4000, World Precision Instruments) equipped with 5 mL syringes (Becton Dickinson) were employed. The syringes were connected to the microfluidic device using Tygon microbore tubing with inner diameter of 0.51 mm (Cole-Parmer). The flow rates were set and the flow was left to stabilise for 15 minutes before any observation was made. The microfluidic device was placed on the stage of an inverted optical microscope (Nikon Ti-U) and the drop formation process was recorded using a Photron Fastcam SA-5. For the droplet sizing experiments the solutions used were dyed with methyl violet, the objective used had a 10× magnification (Nikon Plan Fluor 10X) (2 μm/pixel) and the frame rate selected was 2,000 fps. The recordings contained at least 10 droplet formation events. In the case of the neck kinetics experiments the frame rate selected was 30,000 fps and the objective used had a magnification of 40× (Nikon Plan Fluor 40X) (0.5 μm/pixel). The analysis of the results was carried out using ImageJ software (Schneider et al., 2012). For the droplet sizing experiments the dispersed phase flow rate was kept constant at 5 μL·min^{-1} and the continuous phase flow rate was varied from 5 to 50 μL·min^{-1}, while for the neck kinetics the flow rates were 5 and 25 μL·min^{-1} respectively.

For the GPV experiments the frame rate selected was 30,000 fps and the numerical aperture of the condenser was set to 0.15 < NA_c < 0.25. By reducing the numerical aperture of the

condenser, a speckle pattern can be obtained from the bright field illumination. This is the result of the interference of the light scattered by the nano-tracers that results in the formation of coherence areas, the speckles, with a typical transverse size of $\delta_x = \lambda/NA_C$, where λ is the wavelength of the light. The speckle pattern is obtained from the light scattered from a thin sample volume with a dimension along the axis of observation of $\delta_z = \lambda/NA_C^2$, around the focal plane. For a bright field white microscope light source and the NA_c set at 0.15, the thickness of the volume probed by GPV (δ_z) is thus about 20 μm while the size of the speckles (δ_x) is about 3 μm. The presented results consist of 10 droplet formation events while the errors presented is the standard experimental error. It represents the difference between the measured value and the true value of the measurement and is calculated by

$$E = \frac{\sigma}{\sqrt{N}} \tag{6}$$

where E is the error, σ is the standard deviation and N is the number of observations (Everitt and Skrondal, 2002).

3. Results and discussion

3.1. Droplet sizes in the presence of surfactants

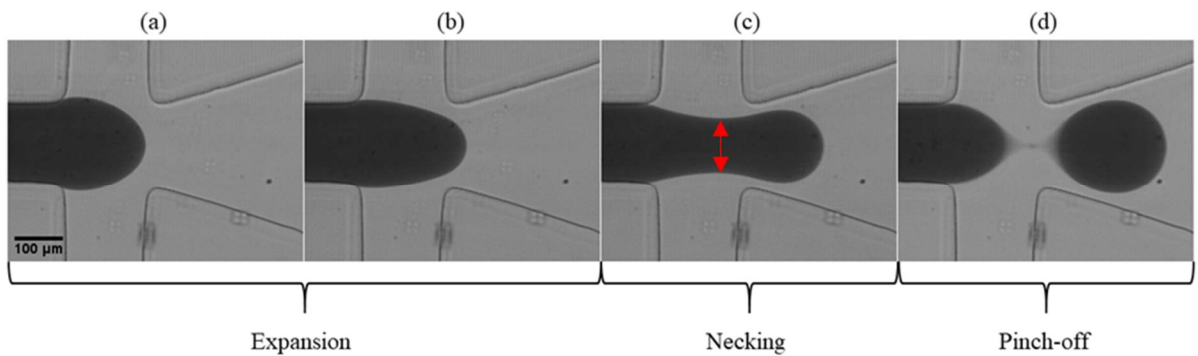Under the current experimental conditions, droplets are formed in the dripping regime (Figure 4).

Figure 4 Droplet formation in a flow-focusing microfluidic device. (a) and (b) expansion, (c) necking, (d) pinch-off. The red line in panel c shows the diameter of the neck during necking.

The size of the studied drops was always smaller than the width of the main channel, therefore drops always had a circular shape in the plane of observation. If the droplet diameter is larger than the channel height, a pancake shape was observed in the experiments. In this case the droplet size refers to the diameter of the drop in the plane of observation.

In the dripping regime the droplet formation process is dominated by the competition between the drag force exerted by the continuous phase and the interfacial tension force resisting the break-up of the interface. Droplets are formed following the expansion, necking and pinch-off stages described previously (Garstecki et al., 2005). In the case of the 96 mPa·s the continuous phase the break-up occurred downstream of the junction in the outlet channel, as in this case the dispersed phase did not retract towards the junction after pinch-off. This can be attributed to the drag from the continuous phase larger than the surface tension force.

A reduction in droplet sizes with an increase in the flow rate of the continuous phase was observed in agreement with literature (Roumpea et al., 2019, Cubaud and Mason, 2008), being the result of an increase of the shear stress acting on the droplet surface. Furthermore, an increase in surfactant concentration leads to a reduction in droplet sizes due to a reduction of the interfacial tension force acting against the break-up (Kovalchuk et al., 2018b). Finally, an increase in the viscosity of the continuous phase also leads to a reduction in droplet sizes, since it will lead to an increase in the drag force per unit of the droplet surface (Cubaud and Mason, 2008).

The effects of all three parameters, flow rate of the continuous phase, interfacial tension and viscosity can be included in the capillary number:

$$Ca = \frac{\mu_c Q_c}{hw\gamma} \tag{7}$$

where μ_c is the dynamic viscosity of the continuous phase, Q_c is the flow rate of the continuous phase, h is the channel height, w is the width of the continuous phase channel and γ is the equilibrium interfacial tension.

The model suggested by (Cubaud and Mason, 2008) was used as a correlation between the drop size and capillary number. This model uses, as an additional parameter, the volume fraction of the continuous phase given by

$$\alpha_c = \frac{Q_c}{Q_c + Q_d} \tag{8}$$

The droplet size normalised by the channel height is presented in Figure 5 as a function of $\alpha_c Ca$. All the data in Figure 5 appears to fall onto a single curve, however, there is a shift to smaller droplet sizes as α_cCa increases.
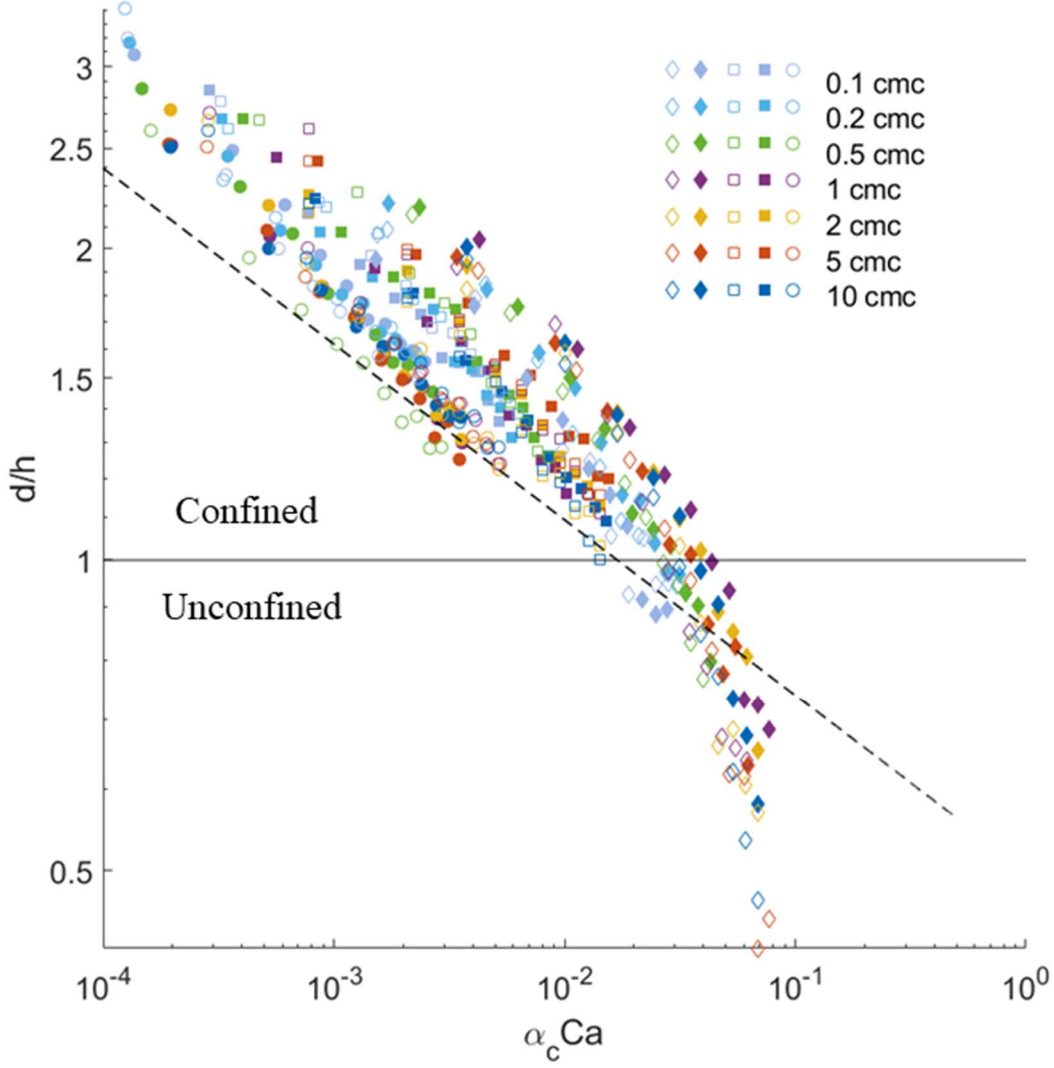
Figure 5 Normalised droplet diameter vs a_cCa for three different continuous phase viscosities. ○: 4.6 mPa·s, □:19 mPa·s, ◇:96 mPa·s. Filled symbols is $C_{10}TAB$, empty symbols is $C_{12}TAB$. Segmented line is the scaling for d/h<2.5 for dripping from literature (Cubaud and Mason, 2008)

To quantify this effect, the data was fitted using the non-linear least squares method for each continuous phase separately. For the 4.6 mPa·s continuous phase, the fit describing the data is $d/h = 0.33\,(a_cCa)^{-0.25}$ and for the 19 mPa·s continuous phase the fit is $d/h = 0.42(a_cCa)^{-0.24}$. For the highest viscosity continuous phase, the droplet sizes follow $d/h = 0.49(a_cCa)^{-0.24}$. In the last case, only the droplet sizes that are larger than the channel height are used for the calculation of the scaling law, i.e. the confined drops. Droplet confinement changes the droplet formation dynamics (Garstecki et al., 2005) and in order to quantify its effect on the droplet size scaling law the confined and unconfined droplets were separated.

Thus, the drop size follows the power law with similar exponent in the whole range of continuous phase viscosities, with the pre-exponential factor slightly increasing with an increase of viscosity.

Literature gives the values 0.5 and -0.17 for the pre-exponential factor and exponent respectively (Cubaud and Mason, 2008). Differences between (Cubaud and Mason, 2008) and the present study are expected due to the different design of the microfluidic devices. Cubaud and Mason used a device with square cross-section, therefore, once reaching the size of the channel, the droplets grow under 2D confinement, i.e. only one dimension, the drop length, increases. In the present study, once a drop reaches a size equal to that of the channel height, 1D confinement applies, i.e. the drop can grow in two dimensions, along the channel length and width. The importance of confinement can be seen from the changes in droplet size for the 96 mPa·s silicone oil. Once the normalised droplet size drops below 1, the power law exponent changes to -0.4. Note, the power law for the droplet volume in this study is $-(0.4)^3 = -0.064$ for unconfined drops since they can grow in three dimentions and approximately $-(0.24)^2 = -0.06$ for the drop under 1D confinement since in this case they are confied in the axis of observation. Therefore, it can be concluded that the drop volume follows similar power law for the unconfined case and 1D confinement. It is difficult to estimate the power law for the drop volume in the (Cubaud and Mason, 2008) study, because the growing drop in their case (drop length between 1 and 2.5 channel size) not only changes its length, but also the shape in the observation plane, but this exponent is obviously considerably larger than 0.06. Thus, it can be assumed that an increase in confinement from 1D to 2D results in an increase of the absolute value of the power law exponent for the drop volume. This can be related to the drastic change in the continuous phase flow by the transition to 2D confinement where the continuous phase can only travel in the corners of the microfluidic device, around the confined droplet, due to the droplet taking up the majority of the channel cross-section. This is referred as corner flow

(Korczyk et al., 2019). In most microfluidic applications, droplet sizes are comparable to the channel height therefore they grow under confinement. The above analysis allows for a better understanding of the importance of confinement during the droplet production process.

Droplet sizes can be affected by dynamic surfactant effects, especially at concentrations below the cmc, however, there is no noticeable deviation from the power law which depends upon surfactant concentration. In particular, for the 4.6 and 19 mPa·s continuous phase viscosities, the droplet sizes fall on a single curve while for the 96 mPa·s a change is observed. During dripping, after the droplet break-up, the interface recoils towards the dispersed phase channel. For very concentrated surfactant solutions above the cmc and for the 96 mPa·s continuous phase, the interface doesn't recoil back, and the break-up occurs closer to the outlet channel.

3.2.   Surfactant mass transport time scales

Mass transfer in the bulk can be facilitated by advection of the fluids, but within the concentration boundary layer diffusion mass transfer is predominant. In the case of non-uniform surface concentration, rearrangement of surfactant molecules over the interface occurs via the adsorption-desorption process, surface diffusion and Marangoni flows. These phenomena are associated with their timescales which should be compared to the droplet formation timescale to examine their relative importance.

The time scale for diffusion limited adsorption, τ_γ, at concentration below the cmc can be estimated as

$$\tau_\gamma = \frac{\Gamma^2}{Dc^2} \qquad (9)$$

Where Γ is the equilibrium adsorption at concentration c and D is the surfactant diffusion coefficient. The equilibrium adsorption for each concentration was calculated by Eq. (2) using

the values of parameters presented in Table 2. The diffusion coefficient can be calculated using (Perkins and Geankoplis, 1969)

$$D_{Am}^o n_m^{0.8} = \sum_{j=1}^n x_j D_{Aj}^o n_j^{0.8} \tag{10}$$

Where D_{Am}^o is the effective diffusion coefficient for a dilute solute A into the mixture ($cm^2 \cdot s^{-1}$), D_{Aj}^o infinite dilution binary diffusion coefficient of solute A into solvent J ($cm^2 \cdot s^{-1}$), x_j molar fraction of j, n_m is the viscosity of the mixture (cP) and n_j is the component viscosity (cP). D_{Aj}^o is given by

$$D_{Aj}^o = \frac{7.4 \times 10^{-8}((\varphi M_j)^{1/2})T}{n_j V_A^{0.6}} \tag{11}$$

Where M_j is the molecular weight of solvent j ($g \cdot mol^{-1}$), T is temperature (K), n_B is the viscosity of the solvent j (cP), V_A is the molar volume of solute A ($cm^2 \cdot mol^{-1}$) and φ is an association factor equal to 2.6 (Perkins and Geankoplis, 1969). The calculated diffusion coefficients are 1×10^{-10} and 9.4×10^{-11} m^2 s^{-1} for the $C_{10}TAB$ and $C_{12}TAB$ respectively. Similar values have been reported experimentaly (Mills, 2016). The diffusion timescale is inversely proportional to concentration, suggesting a rapid replenishment of surfactant in a highly concentrated solution.

The internal flow field of the growing droplet contributes to the redistribution of surfactant molecules during the droplet formation process. This flow mixes bulk solution so the concentration gradient due to surfactant adsorption develops mostly within a thin diffusion boundary layer close to the interface. As to our knowledge, the thickness of diffusion boundary layer resulting from the liquid moving inside the growing drop has not been estimated so far. However for two relevant cases, namely flow around a rigid sphere and inside a cylindrical

pipe on the length scale close to the pipe radius, similar expressions for the thickness of the diffusion boundary layer, δ, were derived in (Levich, 1962):

$$\delta = A \sqrt[3]{\frac{Dr^2}{U}} \tag{12}$$

where D is the diffusion coefficient, r is the sphere/pipe radius, U is the velocity of liquid and A is a constant O(1). Therefore, it can be assumed that the diffusion boundary layer within the forming drop is of the same order of magnitude if the drop surface is retarded. On the same ground the thickness of diffusion boundary layer for the mobile interface should be the same order of magnitude as for external flow around the non-retarded drop (Levich, 1962)

$$\delta \sim \sqrt{\frac{RD}{U}} \tag{13}$$

Considering profiles of interfacial velocity obtained in section 3.4, the interface in this study is mobile. For an average droplet diameter of 240 μm and an average fluid velocity for the growing drop of 4 mm s^{-1} (see section 3.4) the width of the boundary layer is estimated at 1.8 μm. The characteristic time for diffusion through this boundary layer can be estimated by $t_d = \delta^2/D$ and is $\sim$ 30 ms. Note, for mobile interface the characteristic time scale does not depend on diffusion coefficient and is equal to R/U.

Comparison of timescales associated with adsorption layer, t_γ, and diffusion layer, t_d, with drop formation time for concentrations of C$_{12}$TAB 0.1, 0.5 and 1 cmc is given in Figure S.1 of the Supplementary Materials, which shows that t_γ is always smaller than the drop formation time. This means that adsorption is completed on the time scale of droplet formation and the size of the droplets is defined completely by equilibrium interfacial tension.

For C$_{10}$TAB, the cmc value is nearly 4 times larger than for C$_{12}$TAB, therefore it is expected that all drops are formed under equilibrium interfacial tension for this surfactant as well. The

conclusion about drop formation for the two considered surfactants under equilibrium interfacial tension is confirmed by the fact that all data in Figure 5, where the capillary number is based on the equilibrium interfacial tension, fall onto the same curve.

Note, $t_\gamma < t_d$ in the whole range of $C_{12}TAB$ concentration. The same is true for $C_{10}TAB$. Therefore, for the considered surfactants and velocities involved the effect of convective mass transfer on adsorption kinetics can be neglected.

3.3. Neck kinetics

The thinning kinetics of a liquid bridge connecting the forming drop to the bulk of the dispersed phase is dependent upon local phenomena, and thus much more sensitive to surfactant presence and redistribution than the droplet size (Kovalchuk et al., 2018a). For unconfined surfactant-free liquids, kinetics close to pinch-off follow different regimes depending on the physical properties of the fluid undergoing break-up. For small viscosities of the dispersed phase liquid inertia is the main force counteracting the capillary pressure driven thinning. In the case of inertial kinetics the neck diameter, d decreases as (Keller and Miksis, 1983)

$$d = A_I \left(\frac{\gamma}{\rho_d}\right)^{1/3} t^{2/3} \tag{14}$$

Where γ is interfacial tension, ρ_d is the density of the dispersed phase, t is the time remaining to pinch-off and A_I is a constant with values between 1.26-1.4. When the viscous forces dominate, the neck diameter decreases linearly with time (Papageorgiou, 1995),

$$d = A_v \frac{\gamma}{\mu_d} t \tag{15}$$

where A_v is a constant that takes the value 0.1418 and μ_d is the viscosity of the dispersed phase. The cross-over between these regimes is defined by the Ohnesorge number,

$$Oh = \frac{\mu_d}{\sqrt{\rho_d \gamma h}} \qquad (16)$$

where h is the channel height. In this study the Ohnesorge number is $8 \times 10^{-2} \leq Oh \leq 10^{-1}$. Therefore, inertial thinning kinetics are expected.

Very close to pinch-off both inertia and viscosity become important and a transition to the visco-inertial regime is expected (Eggers, 1997, Eggers and Villermaux, 2008) with

$$D = A_{VI} \frac{\gamma}{\mu_d} t , \qquad (17)$$

where A_{VI} a is constant that takes the value 0.0608.

Transition from inertial to visco-inertial regime is expected when the neck diameter and time to pinch-off become of the order of the viscous length, l_v, and time, τ_v, scale respectively

$$l_v = \mu_d^2 / \gamma \rho_d \qquad (18)$$

$$\tau_v = \mu_d^3 / \rho_d \gamma^2 \qquad (19)$$

Taking into account conclusions of the previous section, the equilibrium values of interfacial tension are used to calculate the viscous length and time scale. For the systems used in this study these are $1 \leq l_v \leq 3$ µm and of the order of 10^{-4} ms respectively. The neck diameters and time to pinch-off accessed in this study are larger than the viscous length and time scales and therefore the only observed kinetics should be inertial.

In the case of a break-up occurring inside a viscous continuous phase the neck kinetics may enter the two fluid Stokes regime when the behaviour of the system is dependent on the viscosity ratio between the two fluids (de Saint Vincent et al., 2012). The neck kinetics are described by

$$d = (H\gamma/\mu_c)t \qquad\qquad (20)$$

where H is a constant that can be determined experimentally and depends on the viscosities of the two phases (Cohen and Nagel, 2001). The thinning may enter the Stokes regime when the length scales of interest are in the order of $l_S = (\mu_c/\mu_d)l_v$. For the liquids used in this study l_s is within the observable range only for the most viscous continuous phase of 96 mPa·s with $l_S =$ 16 μm for the surfactant-free dispersed phase and $l_S = 48$ μm for surfactant concentrations above the cmc.

The neck kinetics for $C_{12}TAB$ solutions in 4.6 mPa·s continuous phase are shown in Figure 6. From this part on the results are limited to dispersed and continuous flow rates of 5 and 25 μL·min^{-1} respectively. The neck kinetics for the 19 and 96 mPa·s are presented in Figure S.2 of the Supplementary Materials.
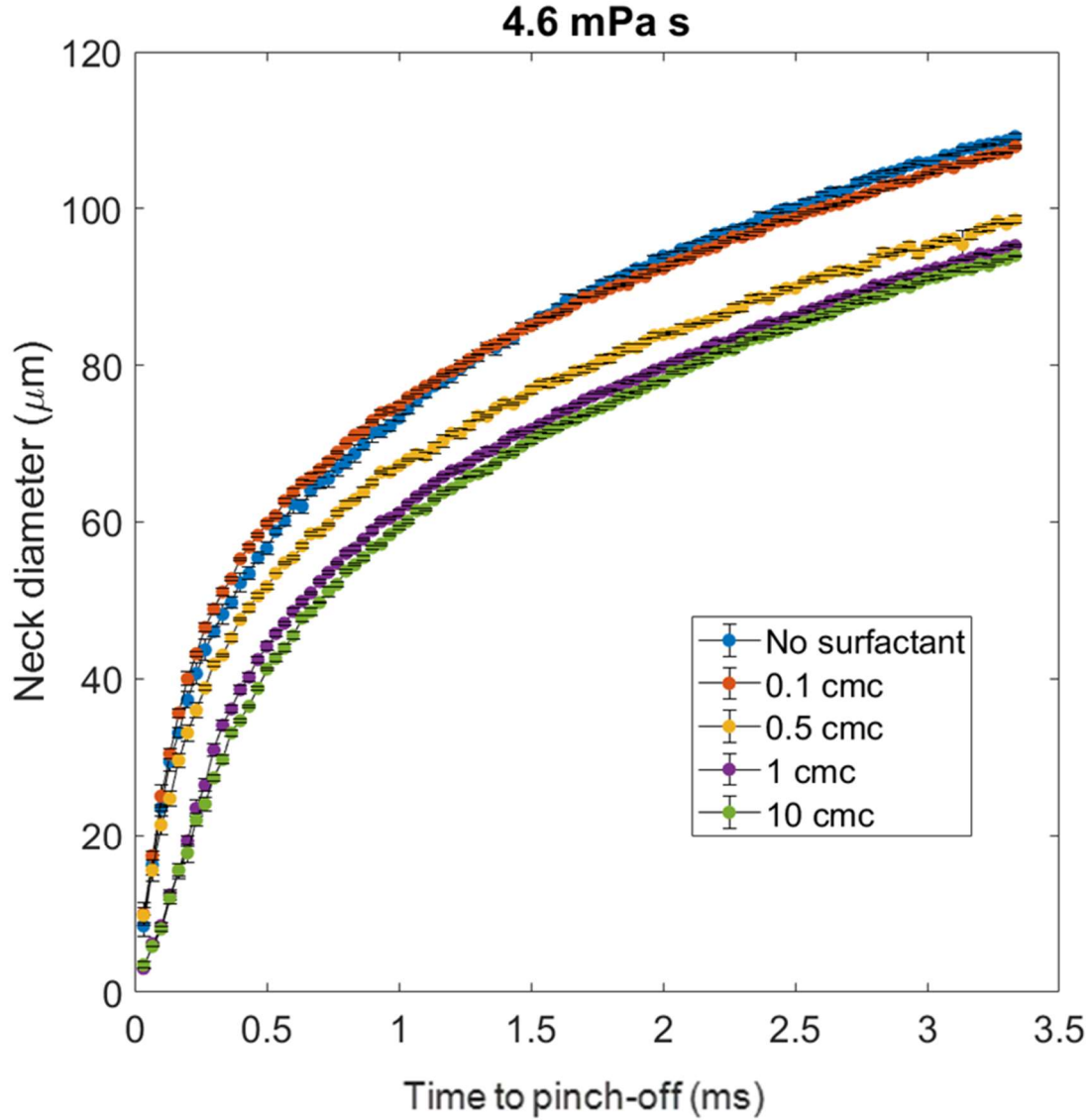
Figure 6 Neck kinetics during necking for $C_{12}TAB$ solutions in 4.6 mPa·s continuous phase.

Figure 6 shows that as the surfactant concentration increases the kinetics slow down and the curves follow the decrease in interfacial tension. The behaviour for the various $C_{10}TAB$ solutions is similar. To examine the thinning rate in more detail, the neck diameter was fitted to a power law, using the non-linear least squares method. For the time scales of necking examined in this study the neck kinetics follow two distinct behaviours. Figure 7 displays the neck kinetics for various $C_{12}TAB$ solution for $0.5 \leq t \leq 3$ ms. The *d(t)* dependence is linear on log/log scale at $t > 1$ ms for all surfactant concentrations confirming that the neck kinetics follow a power law with an exponent increasing with an increase of surfactant concentration.

The slope of the *d(t)* curves begins to increase at $t < 1$ ms demonstrating an increase in the power law exponent. The capillary instability is responsible for the neck thinning. The kinetics predicted by the Ohnesorge number dictate a thinning exponent of 2/3 which is not reached in the timescales examined in this study. This can be caused by the presence of retarding factors such as droplet confinement and the flow of the dispersed phase. The increase of the thinning exponent at t < 1 ms can be caused by the decreased contribution of such retarding factors in the development of the capillary instability.
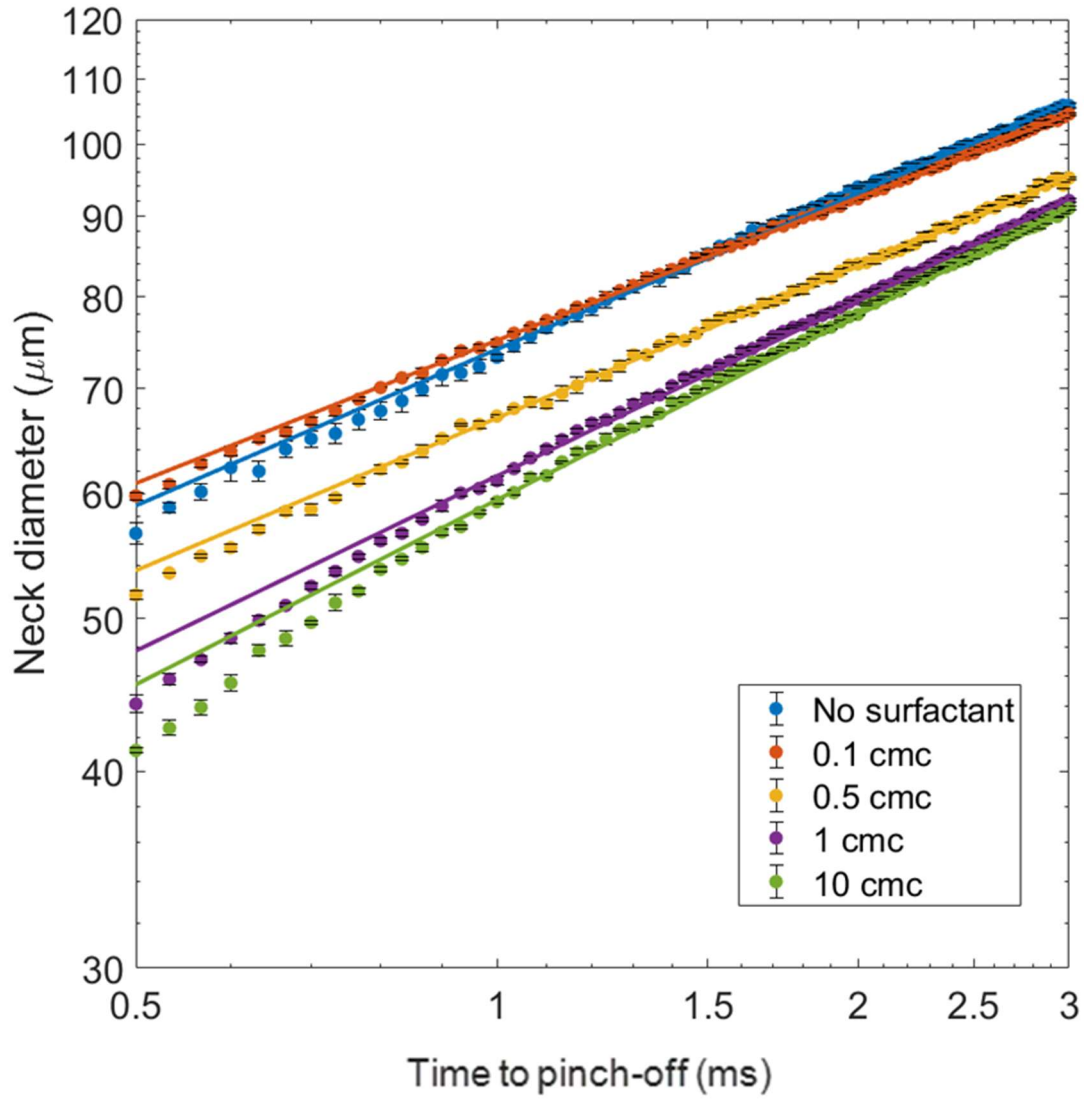

Figure 7 Neck kinetics for various $C_{12}TAB$ solutions for $0.5 \le t \le 3.3$ ms. Continuous phase is 4.6 mPa·s silicone oil. Straight lines present the power law fitting for $1 < t < 3$ ms.

The smallest values of exponent, around 0.3, were observed for the surfactant free dispersed phase. For solutions below the cmc the thinning exponent increases as the surfactant concentration increases and it appears to level off once the cmc is reached at values reaching 0.4 for viscosities of continuous phase 4.6 and 19 mPa·s. For continuous phase of 96 mPa·s the maximum value of exponent is below 0.6. As discussed above, the neck kinetics should be inertial and a constant exponent value of 2/3 is expected. The very considerable deviation of the exponent values from the predicted by inertial kinetics can be due to the fact the break-up occurs in a confined geometry. The decrease in the rate of the neck thinning was earlier observed and explained for bubble formation in microfluidic device with geometrical flow focusing (Garstecki et al., 2005). It was suggested in (Garstecki et al., 2005) that geometrical confinement stabilises the thread against capillary instability and the neck thinning is mediated by fluid flows and pressure gradients imposed. Stabilisation of a liquid thread under geometrical confinement was reported in (Humphry et al., 2009), who showed that, depending on confinement, the jet can be completely stable or the growth rate of instability can be considerably reduced (Son et al., 2003).

Figure S.3 shows that the neck kinetics exponent reaches values close to 2/3 only for the 96 mPa·s continuous phase and for solutions above the cmc, where the normalised droplet diameter plotted in Figure 5 is below unity and thus the droplets are unconfined. It can therefore be postulated that an increase in the exponent with an increase of surfactant concentration and an increase of continuous phase viscosity is due to decrease of the drop size and therefore the decrease of confinement.

There is no considerable difference in the exponent values for $C_{10}TAB$ and $C_{12}TAB$, because as was demonstrated in the previous section the drop formation occurs under conditions of

equilibrium interfacial tension. Note, the equilibrium interfacial tension at the same concentrations in terms of cmc is similar for both surfactants (Figure 1).

In the case of the 4.6 mPa·s silicone oil, the thinning exponent for solutions below the cmc is in the range of the solution without surfactant. As the concentration reaches the cmc the thinning exponent remains steady for different surfactant concentrations suggesting a constant interfacial tension and drop size. With an increase of the viscosity of the continuous phase, the concentration at which the deviation from the behaviour of the surfactant free solution is observed decreases. For silicone oil with a viscosity of 96 mPa·s, the exponents for all surfactant solutions are higher than for the surfactant free solution. It can be concluded that for the drop size larger than certain critical value the contribution of capillary instability in the kinetics of the neck thinning is negligible. For these drops, the neck thinning exponent remains the same, around 0.3. With an increase of surfactant concentration and a decrease of drop size, effect of capillary instability increases, resulting in the growth of the thinning exponent.

The thinning exponent begins to grow at $t < 1$ ms demonstrating an increased contribution of the capillary instability in the neck kinetics. Figure 8 demonstrates a further increase in the slope of $d(t)$ for the surfactant-free dispersed phase on a log-log scale for a continuous phase of 4.6 and 19 mPa·s with a thinning exponent reaching the value around 0.55 for 4.6 mPa·s oil and around 0.58 for 19 mPa·s oil. These exponent values show that a self-similar solution was not reached on the timescale of this study and therefore Equation 9 cannot be used for quantitative analysis of the thinning kinetics.
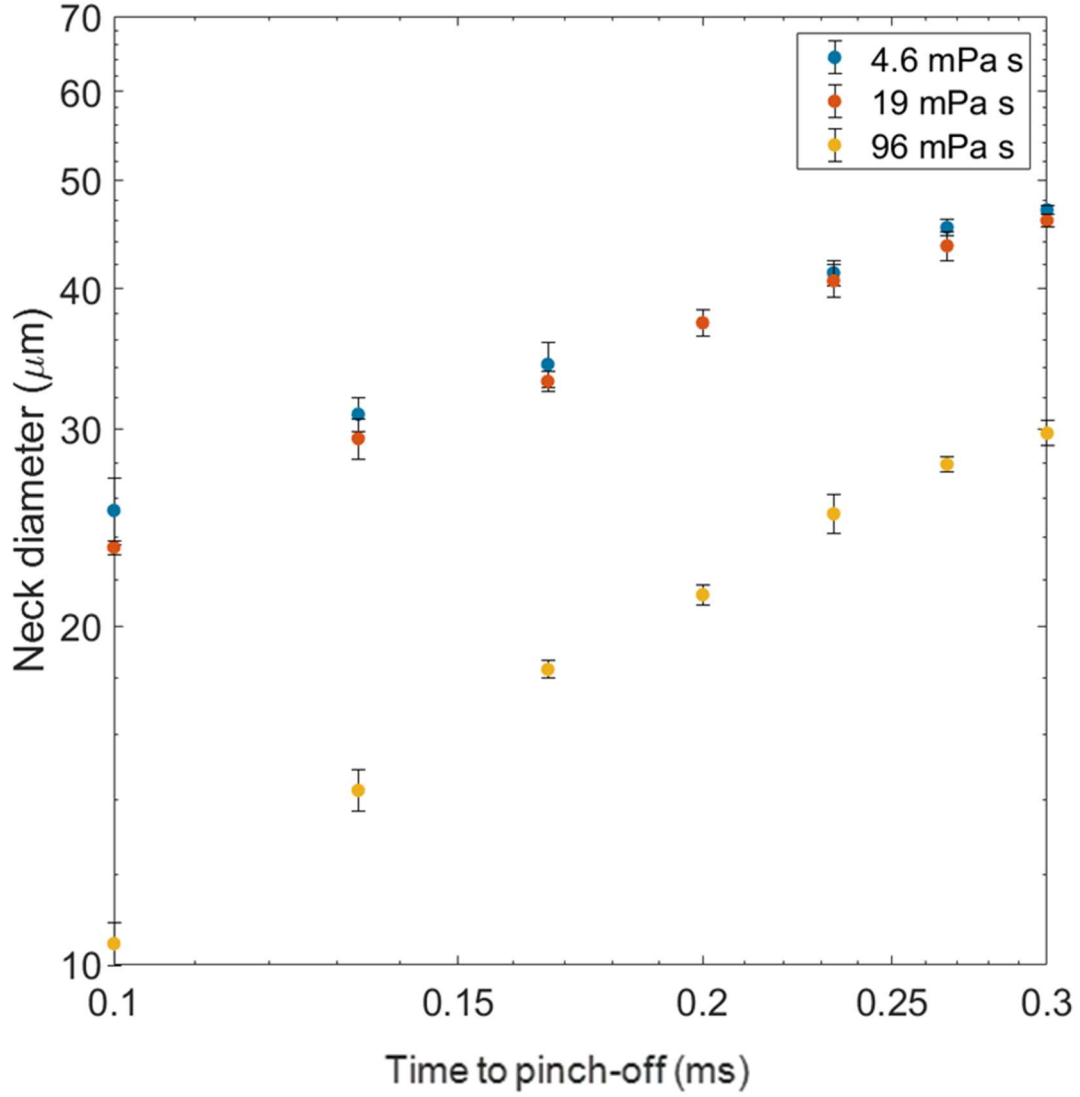
Figure 8 Short time neck kinetics for surfactant free system in the three continuous phases studied

Figure 9 shows that *d(t)* demonstrates a linear behaviour for continuous phase of 96 mPa·s, at

d < 28 μm with the thinning exponent being 1.03±0.3. This is in line with the assumed

appearance of the two fluid Stokes regime. With an increase of surfactant concentration, the

slope of *d(t)* decreases (left panel of Figure 9) with the decrease of interfacial tension and levels

off at *c* ≥ cmc. The difference in the line positions in the left panel of Figure 9 is due to

experimental error in definition of pinch-off time (within time between two frames). For the

same reason, the values of the neck diameter for the two frames closest to pinch-off are

excluded from consideration. The right panel of Figure 9 displays the equilibrium interfacial

tensions of C_{12}TAB solutions presented in Figure 2 compared to the calculated interfacial tensions using the two fluid Stokes model for the final stages of the break-up.
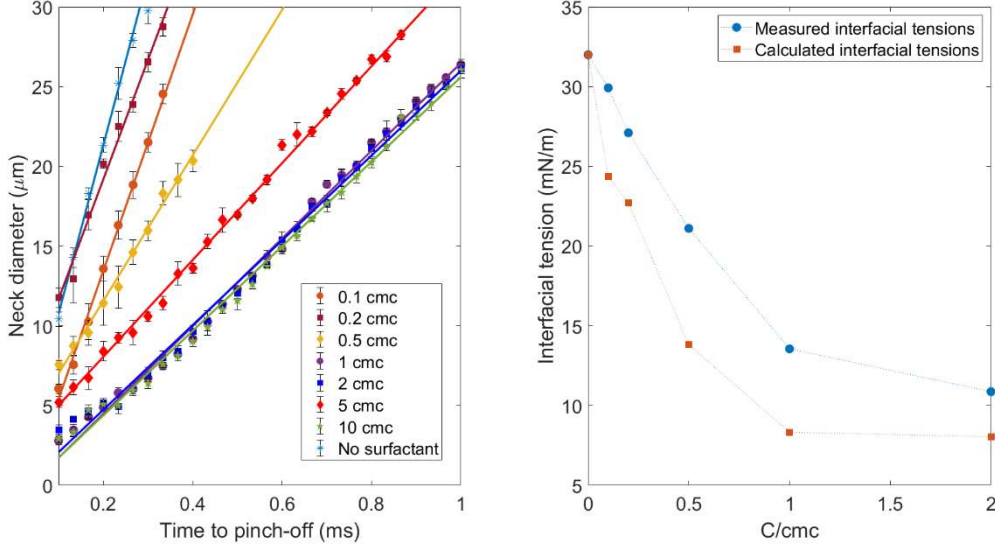

Figure 9 Thinning kinetics close to pinch-off (left panel) and comparison the effective and measured equilibrium interfacial tension (right panel) for C_{12}TAB solution in 96 mPa·s silicone oil.

Using the slope of the surfactant free case the constant *H* in equation 15 can be calculated as 0.32 which is in line with the predicted value of 0.3 from literature (Cohen and Nagel, 2001). Figure 9 shows that the calculated interfacial tensions are smaller than the measured equilibrium interfacial tensions. This suggests that the process evolution is slower than expected in the final stages for capillary pressure based on equilibrium interfacial tension, which can be caused by Marangoni stresses and the redistribution of surfactant on the thinning neck (Kovalchuk et al., 2017).

3.4. Hydrodynamics during droplet formation

The 2-D velocity field in the liquid bridge during the necking stage in the middle plane of the microfluidic device was measured by GPV and is shown in Figure 10. As the necking stage begins, velocities are low and the maximum values are recorded in the centre of the neck (Figure 10a, b). As the neck diameter decreases, the capillary pressure here increases, forcing

the liquid to flow out of the neck. This increases the velocity of the fluid moving through the neck towards the expanding droplet, whilst a stagnation zone is formed at the base of the neck on the side of the dispersed phase channel, Figure 10c. At this point the pressure provided by the syringe pump is still larger than the capillary pressure in the thinnest part of the neck and initially fluid bypasses this low velocity zone and moves towards the outlet channel. As the thinning process progresses, the capillary pressure increases, and fluid is no longer moving towards the outlet channel but is expelled from the neck to both sides, Figure 10d. The resolution of GPV is determined by the size of the speckles (Alaimo et al., 2006). The size of the speckles is determined by the maximum scattering angle and the wavelength of light source ($\sim\lambda/2\theta_{max}$). For particles with sizes smaller than the incident light wavelength, such as in this study, the maximum scattering angle is determined by the numerical aperture of the collection optics ($\theta_{max} \sim NA_c$). Therefore, the size of the speckles produced in this study, for a microscope light source with a mean wavelength of 500 nm and the NA_c set at 0.15, is approximately 3 μm which determines the spatial resolution of the technique.
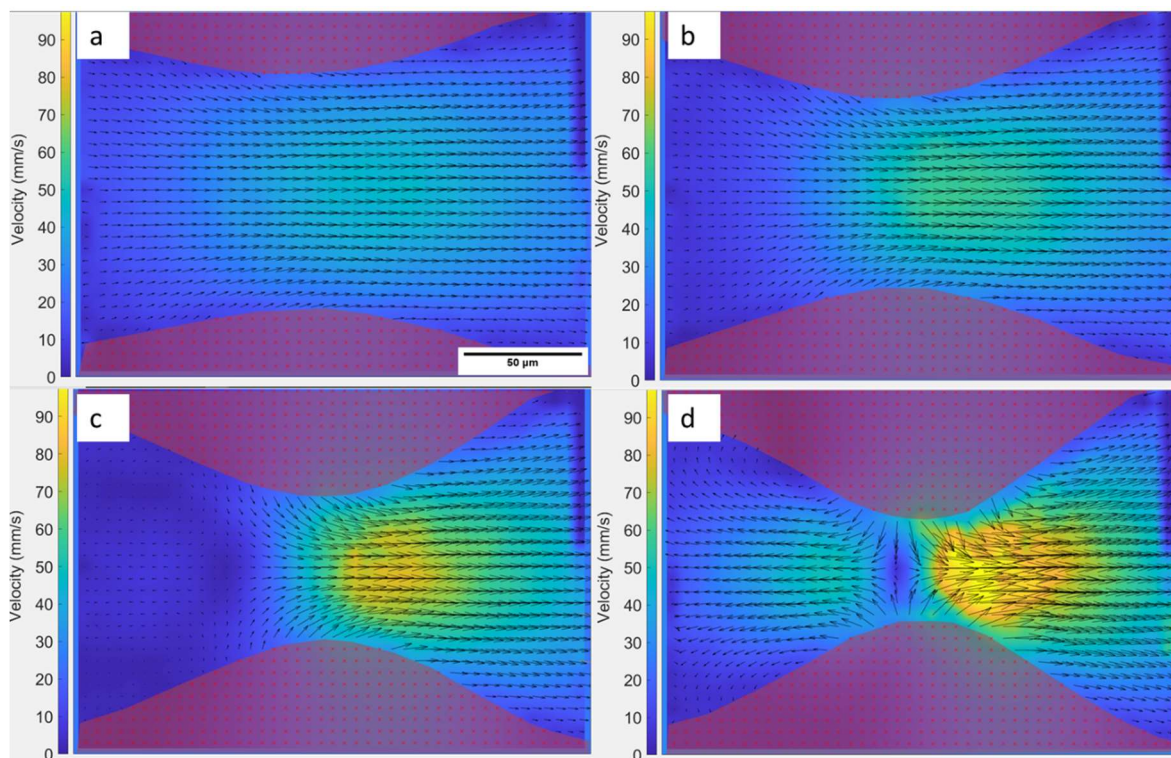
Figure 10 Velocity fields during necking for a 0.1 cmc (2 mM) $C_{12}TAB$ solution. Continuous phase is 4.6 mPa·s silicone oil. Neck diameter is a: 100, b:80, c: 60 and d:40 μm.

These results are in agreement with experimental studies on emulsification using micro-PIV (Roumpea et al., 2019). When the viscosity of the continuous phase increases, the necking process follows the same steps, but the velocities close to the interface reduce (Figure S.4). A reversal of the flow along the interface, with negative velocity values, on the side of the bridge closer to the dispersed phase channel, is observed for the 4.6 mPa·s continuous phase. The interfacial flow reversal at the same neck diameter becomes smaller in magnitude for the 19 mPa·s and then vanishes completely for the 96 mPa·s continuous phase. In the bulk of the dispersed phase reversal of the flow is observed for all thinning necks.

It was demonstrated (Figure 7, 9) that in the presence of small quantities of surfactant the thinning neck displays a behaviour very similar to a surfactant free system. The normalised velocities along the interface for these solutions are compared in Figure 11. The interface is normalised using the length over which the velocities are extracted which in each case is the

length of the interface while the fluid velocity (U_M) used to normalise the velocity close to the interface is the maximum fluid velocity at the thinnest part of the neck for each diameter.
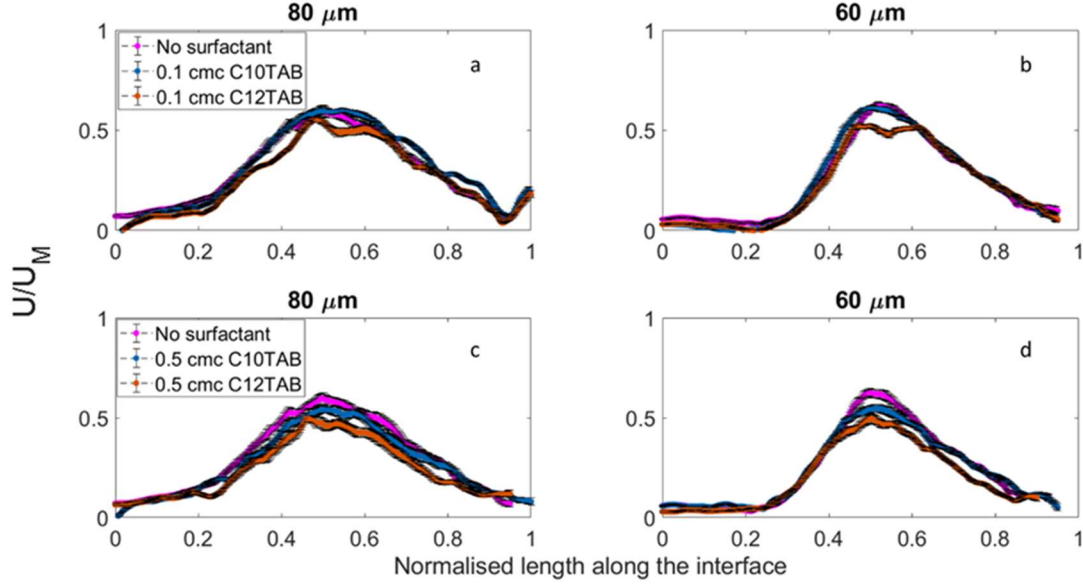

Figure 11 Normalised velocity profiles along the interface of the thinning bridge. Surfactant concentrations: a, b: 0.1 cmc, c, d: 0.5 cmc. Continuous phase is 4.6 mPa·s silicone oil. Maximum velocities of dispersed phase used for normalisation are: panel a - 62.76, 54.1 and 60.43 mm s^{-1}, panel b - 78.86, 73.8 and 75.31 mm s^{-1}, panel c - 62.76, 48.69 and 54.26, panel d - 78.86, 61.95 and 70.86 mm s^{-1} for the no surfactant, C$_{10}$TAB and C$_{12}$TAB respectively. The length of the interfaces in panel a are 202, 196 and 214 μm for the surfactant free, 0.1 cmc C$_{10}$TAB and 0.1 cmc C$_{12}$TAB. For panel b these are 230, 217 and 225 μm. 202, 195 and 203 μm for panel c. And 230, 198 and 208 μm for panel d.

For surfactant concentration 10 times smaller than the cmc the maximum velocity for a solution of C_{12}TAB is only slightly smaller than the velocity in the surfactant-free neck, whereas there is a noticeable decrease in the maximum velocity for C_{10}TAB solution. It can be assumed therefore that there is a considerable depletion of surfactant from the neck region for C_{12}TAB, but not for C_{10}TAB. The dimensionless velocity profiles for surfactant-laden solutions are very similar to the surfactant free system throughout the process (Figure 11a and b) suggesting that there is no additional surface retardation in surfactant solutions. However, the slightly smaller normalised surface velocity of C_{12}TAB solution can be indication of a Marangoni stress due to surfactant depletion from the neck region. This can be examined by comparing the interface deformation timescale to the adsorption timescale. The interface deformation timescale can be defined as

$$t_{def} = \frac{L}{U_{max} - U_{min}} \tag{21}$$

Where U_{max} and U_{min} are the maximum and minimum fluid velocities close to the interface for a specific neck diameter and L is the length of the interface over which the velocity changes from min to max. For the C_{12}TAB the deformation time scale is between 2.1 and 4.4 ms, 2.8 and 5.3 ms and 2.3 and 5.8 ms for the 4.6, 19 and 96 mPa·s continuous phase respectively. Increasing the surfactant concentration leads to an increase in the deformation timescale due to the reduction of the velocities along the interface. For the 0.5 cmc C_{12}TAB this timescale is between 2.5 and 4.2 ms, 3 and 6.6 ms and 3.3 and 9.3 ms for the 4.6, 19 and 96 mPa·s continuous phase respectively. The interface deformation timescales for the C_{10}TAB solutions are similar. For solutions with surfactant concentrations equal to 0.5 times the cmc the ratio between the velocities along the interface and the maximum fluid velocities seems to be smaller (**Error! Reference source not found.**Figure 11 c and d). Increasing the surfactant concentration reduces interfacial tension which reduces the capillary pressure that drives the neck thinning. This in turn reduces the maximum fluid velocity.

The smaller ratios indicate that the interfacial velocities are smaller as well suggesting the presence of Marangoni stresses on the interface acting against fluid flow. The adsorption timescale for C_{12}TAB is 3.1, 2.5 and 1.5 ms for solutions of 0.1, 0.2 and 0.5 cmc respectively. This timescale is in the same order of magnitude as the droplet deformation timescale suggesting that the thinning process might evolve under non-equilibrium conditions especially close to pinch-off when the flow from the neck accelerates considerably. In contrast, a 0.1 cmc solution of C_{10}TAB displays an adsorption timescale of 0.14 ms which is significantly smaller than the deformation timescale.

An example of the interfacial velocities during the break-up in the 19 mPa·s continuous phase is presented in Figure 12.
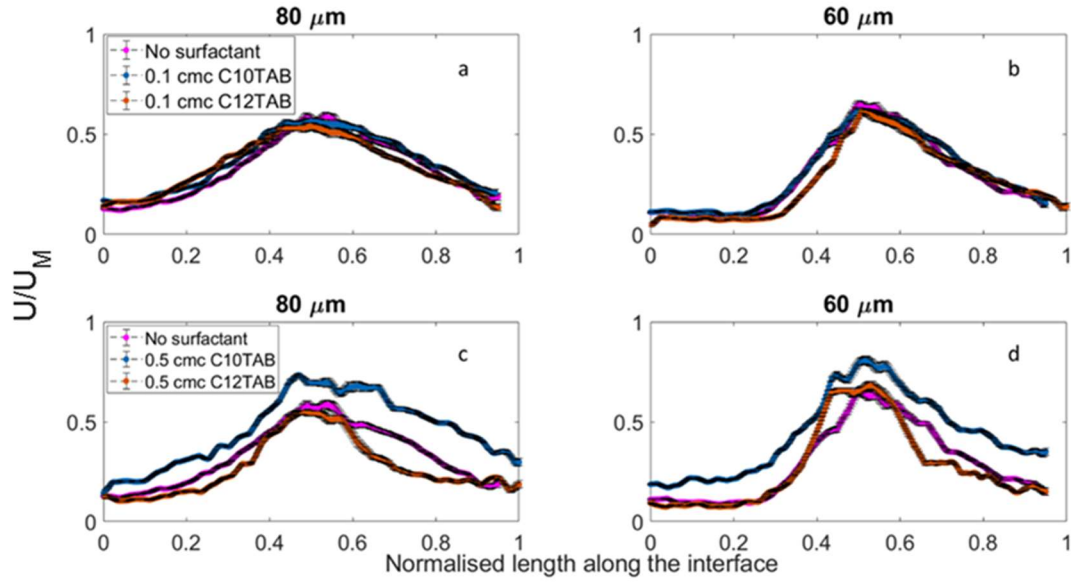
Figure 12 Normalised velocity profiles along the interface of the thinning bridge. Surfactant concentrations: a, b: 0.1 cmc ; c, d: 0.5 cmc. Continuous phase is 19 mPa·s silicone oil. Maximum fluid velocities are: panel a - 53.4, 49.05 and 48.15 mm s^{-1} , panel b: 64.35, 62.7 and 63.3 mm s^{-1} , panel c: 53.4, 37.5 and 41.25 mm s^{-1} , panel d - 64.35, 44.85 and 45.9 mm s^{-1} for the no surfactant, C_{10}TAB and C_{12}TAB system respectively. The length of the interfaces in panel a are 224, 221 and 226 μm for the surfactant free, 0.1 cmc C_{10}TAB and 0.1 cmc C_{12}TAB. For panel b these are 231, 237 and 235 μm. 224, 220 and 214 μm for panel c. And 231, 223 and 220 μm for panel d.

For solutions with concentration 10 times lower than cmc the behaviour is similar to the case of 4.6 mPa·s continuous phase, but the maximum velocities are smaller due to slower neck thinning. The normalised surface velocity profiles are very close to the velocities of a surfactant free system, whereas maximum velocities for surfactant-laden solutions are slightly lower. In the case of surfactant concentration of 0.5 times the cmc the normalised interfacial velocities for the C_{10}TAB solution are larger in comparison to the case of C_{12}TAB and surfactant-free drop. The maximum fluid velocities for Figure 12 c and d are very close for the C_{10}TAB and C_{12}TAB and are much smaller compared to the surfactant-free dispersed phase, demonstrating the presence of similar amounts of surfactant on the neck surface. The difference in normalised surface velocities can be attributed to Marangoni stresses reducing the fluid velocities along the interface. The interface deformation timescale remains similar to the adsorption timescale for the 0.1, 0.2 and 0.5 cmc C_{12}TAB solutions. The only plausible explanation for the noticeably larger surface velocity of C_{10}TAB solution in Figure 14 c, d, is that the neck surface

displays smaller velocities for all cases presented in Figure 13 and those in Figure 14 a,b. The retardation in the surfactant-free case can be due to the traces of surface active impurities. It can be assumed that the interface can be remobilised for the case of $C_{10}TAB$ solution due to large molecular concentration of this surfactant and slower neck kinetics in 19 mPa·s continuous phase.

The expansion stage of the droplet formation process is examined for surfactant free (Figures 13, 14) and surfactant-laden (Figs. 15, 16) systems. The velocities are extracted from the middle plane of the growing drop. In each panel the flow field is presented in the frame moving along the x-axis with the velocity equal to the average velocity within the drop.

The fluid moves into the droplet due to the action of the syringe pump. It was documented in literature that as the droplet grows into the main channel, liquid is transported mainly along the sides of the droplet (Pirbodaghi et al., 2015). The motion of the continuous phase affects the flow pattern inside the dispersed phase (Timgren et al., 2008), because the fluid closer to the interface experiences the drag of the continuous phase, which can be retarding near the channel walls and accelerating along the corners of the channel. Interaction with complex flow field of continuous phase can result in 3-dimensional flow patterns inside the growing drop where the middle plane flow is diverted towards the bottom and top of the expanding droplet. (Kinoshita et al., 2007).
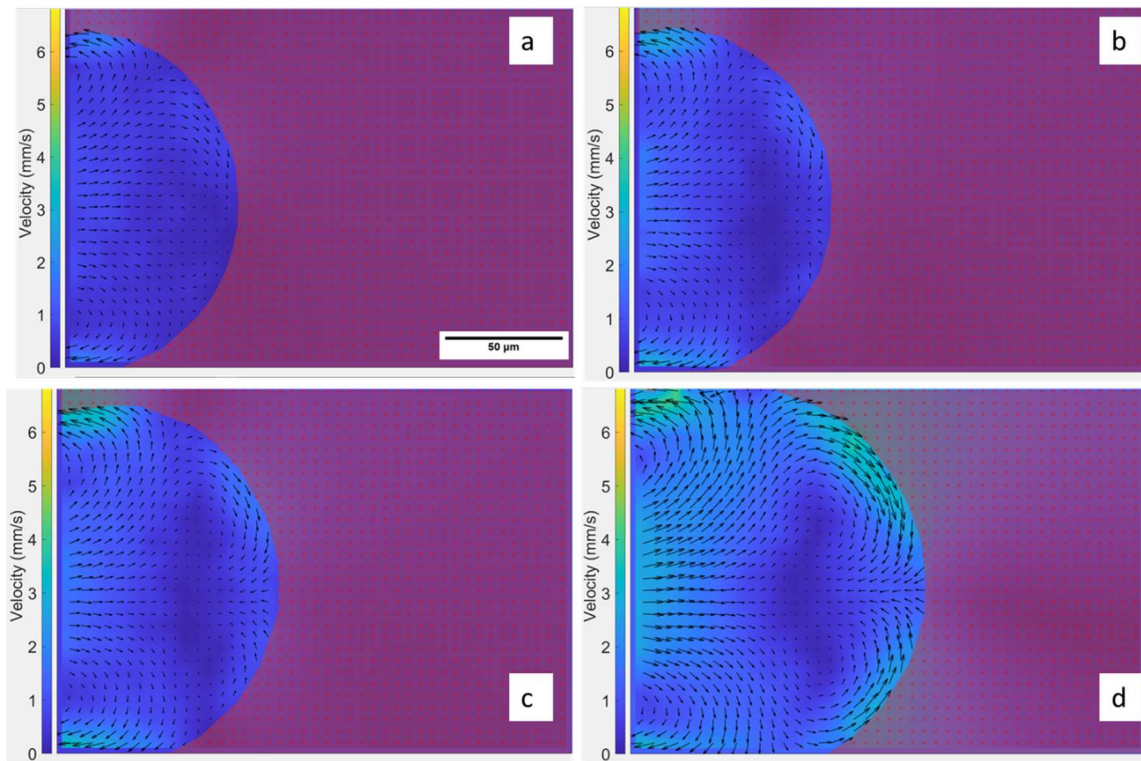
Figure 13 Expansion stage of a surfactant free system. The continuous phase is 4.6 mPa·s silicone oil. a: 3.3 ms b: 6.6 ms. c:10 ms. d: 13.2 ms after the previous droplet pinch-off. Average velocity subtracted is 2.4, .3.5, 4.4 and 4.6 mm/s for frames a, b, c and d, respectively

At the beginning of the expansion stage, the velocities are small and increase as the process develops. The flow of the continuous phase is faster than the flow of the dispersed phase in the corners (not seen in the middle plane) and, after diverging from the corners at the front of the drop. This flow accelerates the flow in the dispersed phase close to the surface. The decelerating effect of continuous phase close to the walls results in the large negative velocity close to interface in the rear part of the drop.
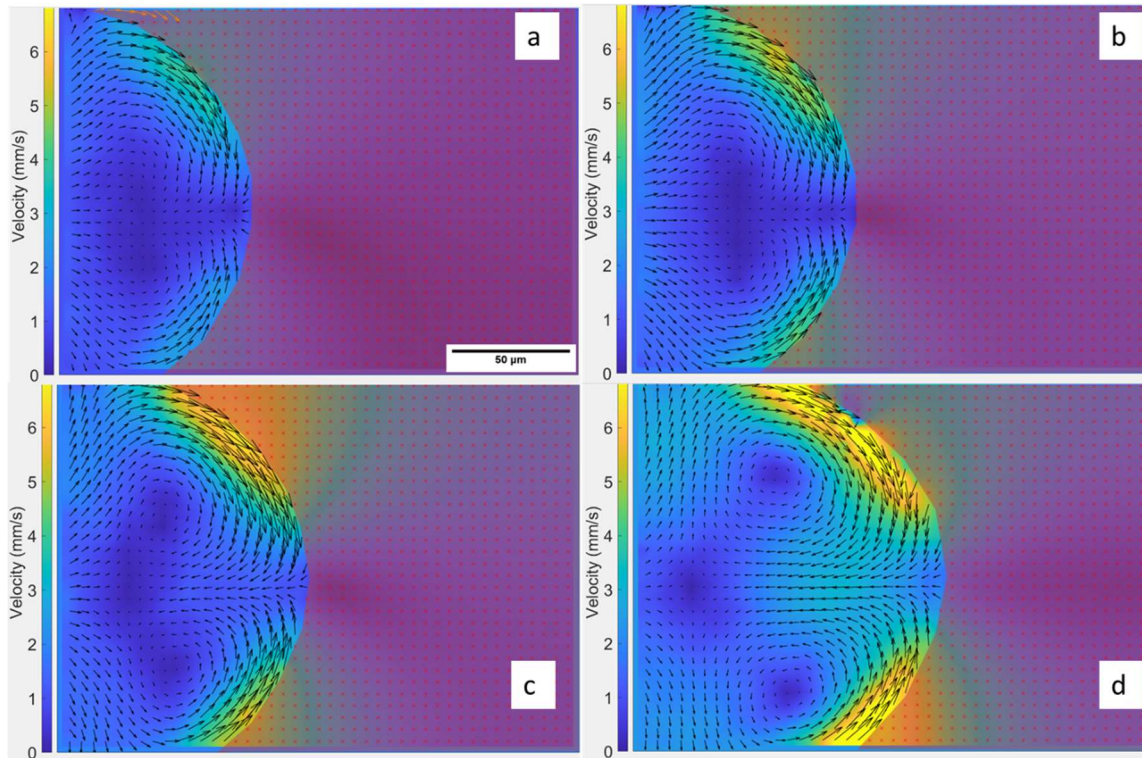
Figure 14 Expansion stage of a surfactant free system. Continuous phase is 19 mPa·s silicone oil. a: 3.3 ms b: 6.6 ms. c:10 ms. d: 13.2 ms after the previous droplet pinch-off. Average fluid velocity subtracted is 4.1, 4.2, 4.9, 3.9 mm/s for frames a, b, c and d respectively

In contrast to necking, the velocities close to the interface increase as the continuous phase viscosity increases as shown in Figure 14. Increasing the continuous phase viscosity increases the drag force exerted by the continuous phase on the dispersed phase (Husny and Cooper-White, 2006). The increase of the drag force along the interface increases the shear stress on the interface. This increase in shear stress leads to an increase in the dispersed phase velocity. Furthermore, two recirculation zones are formed near the tip of the drop as the expansion stage progresses. In the case of the 96 mPa·s continuous phase a similar behaviour is observed. The velocities are in the same order of magnitude as in the case of 19 mPa·s continuous phase and the same recirculation zones are formed.

At the first stages of expansion a low velocity zone forms at the tip of the droplet. As the droplet expands fluid moves around that zone and this lower velocity area is moved to the centre of the expanding droplet as the process advances. In the cases of more viscous continuous phases

a different behaviour is observed. Initially a small recirculation zone is formed at the tip and centre of the expanding droplet. As the process advances this zone separates into two recirculation zones (Figure 14 a, b), one at each side of expanding droplet and a stagnation zone is formed at the base of the expanding droplet. That stagnation zone is formed where the fluid recirculating from the tip to the centre of the drop meets the dispersed phases coming into the drop due to the action of the pump.
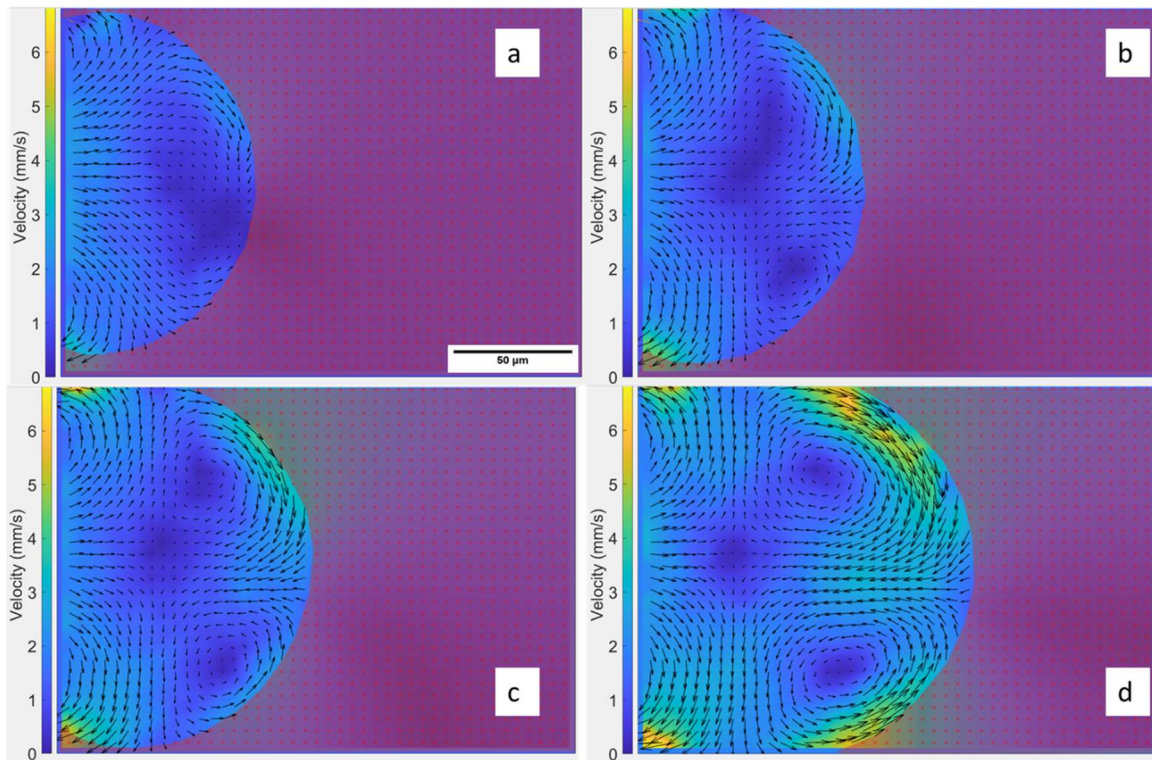

Figure 15 Expansion stage of a 0.5 cmc C₁₀TAB solution. Continuous phase is 4.6 mPa·s silicone oil. a: 3.3 ms b: 6.6 ms. c:10 ms. d: 13.2 ms after the previous droplet pinch-off. Average velocity subtracted is 4.9, 4.2, 4.3 and 4.6 mm/s for frames a, b, c and d respectively

In the case of a surfactant free system during droplet formation in 4.6 mPa·s silicone oil no significant recirculation is observed. In contrast, in the case of a surfactant-laden system (Figure 15), the formation of two recirculation zones similarly to the cases of higher viscosity continuous phase for a surfactant free system is observed. In a recent study (Roumpea et al., 2019) recirculation was observed only in a surfactant free system. The absence of recirculation in systems with surfactant was attributed to the accumulation of surfactant at the tip of the

expanding droplet that creates Marangoni stresses along the interface (Roumpea et al., 2019). The difference in the flow patterns with the present study is due to difference in the channel shape (rectangular in the present study and rounded in the study of (Roumpea et al., 2019)) and the difference in flow velocities. The flow velocities in the present study are nearly an order of magnitude smaller therefore creation of retarding concentration gradients during the expansion stage is less likely.
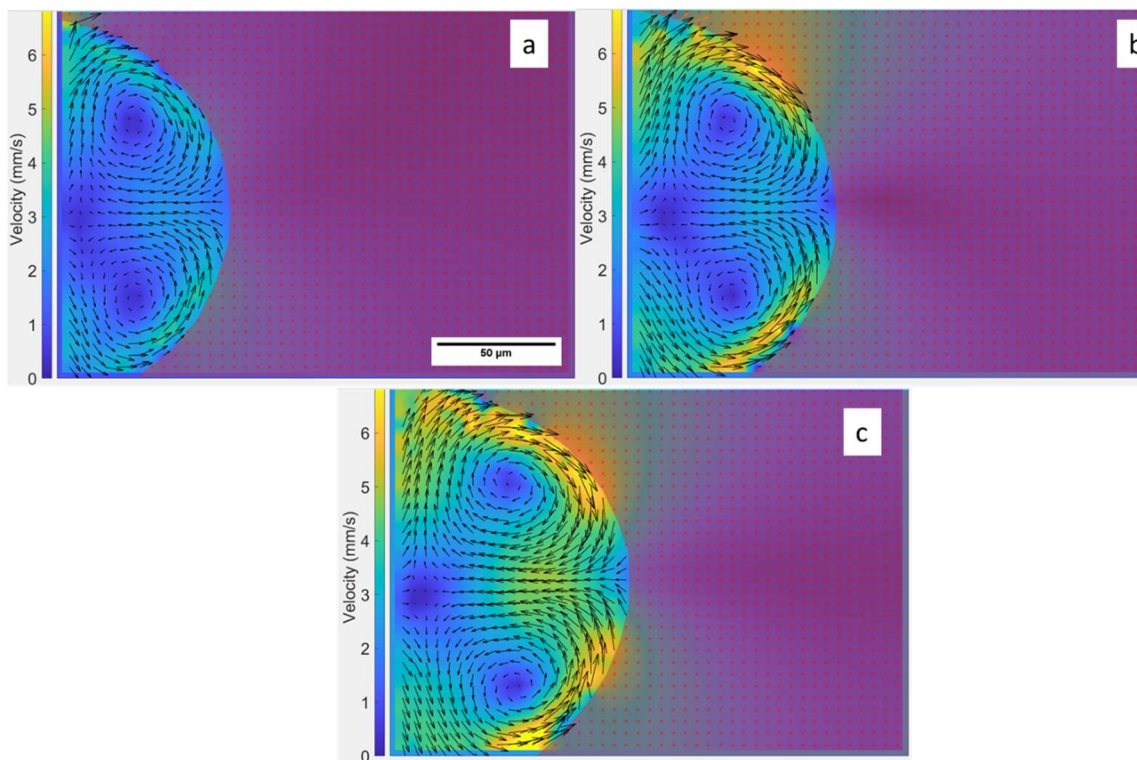

Figure 16 Expansion stage of a 5 cmc $C_{10}TAB$ solution. Continuous phase is 4.6 mPa·s silicone oil. a: 3.3 ms b: 6.6 ms. c: 10 ms after the previous droplet pinch-off. Average fluid velocity subtracked is 5.3, 5.5 and 5.2 mm/s from frames a, b and c respectively.

The formation of two recirculation zones and a stagnation zone, present from the first stages of expansion, is observed also for solution of $C_{10}TAB$ with surfactant concentration 5 cmc (Figure 16). Increasing the continuous phase viscosity leads to similar recirculation patterns in all surfactant solutions.

4. Conclusions

The drop formation process and 2-D velocity profiles were studied using a flow focusing microfluidic device operating in the dripping regime using a water/glycerol solution as the dispersed phase and various silicone oils as the continuous phase. GPV was used to investigate the velocity fields during the expansion and necking stage of the droplet formation process.

It was found that the addition of surfactant, the increase in continuous phase flow rates and viscosities, decreases the size of the produced droplets. Plotting the normalised droplet diameter against the the capillary number based on the continuous phase, the droplet sizes fall on a single curve. The proposed scaling law changes drastically when the droplet formation is unconfined.

The neck kinetics were studied for surfactant-free and surfactant-laden systems. The Ohnesorge number predicts inertial kinetics, but due to droplet confinement the thinning exponent is smaller for time scales 1 ms < t < 3 ms. Only when the break up occurs within the 96 mPa·s continuous phase, and the droplet diameter is smaller than the channel height, does the exponent approach the predicted value. The thinning exponent depends on surfactant concentrations and, for solutions below the cmc, the thinning exponent of surfactant systems is in the range of that for a surfactant free solution. The exponent increases as the surfactant concentration increases. As the neck pinch-off approaches, for t < 1 ms, the thinning exponent grows but does not reach the value predicted for the self-similar solutions in the case of 4.6 and 19 mPa·s continuous phase. For the case of 96 mPa·s continuous phase the neck kinetics at t < 1 ms and for neck diameters below 28 μm follows the two fluid Stokes regime. The calculated experimental value of the constant H used in the model, 0.32, is comparable to the predicted literature value. Furthermore, the calculated interfacial tension is slightly smaller than the

equilibrium values suggesting that the process can evolve under non equilibrium conditions of retarding Marangoni stresses.

GPV allowed for the resolution of the velocity field demonstrating the effect of Marangoni phenomena on interfacial flows. The velocity profiles during necking showed that the fluid velocity increases as the neck thins. As the neck diameter decreases a flow reversal is observed on the side of the neck close to the dispersed phase channel. The velocities along the interface increase as the neck diameter decreases and the velocity magnitude is smaller for higher continuous phase viscosities. When a surfactant with slower adsorption dynamics is present, such as $C_{12}TAB$, velocities along the interface appear to be smaller suggesting the presence of Marangoni stresses along the interface of the thinning neck. During the expansion stage it was found that increasing the continuous phase viscosity leads to larger internal recirculation in the growing droplet. In the case of 4.6 mPa·s no recirculation is observed for the surfactant free case while the addition of surfactant leads to the formation of two recirculation zones. These are caused by the liquid flow along the interface meeting at the tip of the expanding droplet and converging inwardly and encountering the liquid pushed forward by the syringe pump.

Acknowledgements

References

AKSENENKO, E. V. 2001. 7. Software tools to interpret the thermodynamics and kinetics of surfactant adsorption. *Studies in Interface Science.* Elsevier.
AKSENENKO, E. V. 2021. Available: http://www.thomascat.info/Scientific/adso/adso.htm. [Accessed].
ALAIMO, M., MAGATTI, D., FERRI, F. & POTENZA, M. 2006. Heterodyne speckle velocimetry. *Applied physics letters,* 88**,** 191101.

ALVAREZ, N. J., VOGUS, D. R., WALKER, L. M. & ANNA, S. L. 2012. Using bulk convection in a microtensiometer to approach kinetic-limited surfactant dynamics at fluid–fluid interfaces. *Journal of colloid and interface science,* 372**,** 183-191.

ANNA, S. L. 2016. Droplets and Bubbles in Microfluidic Devices. *Annual Review of Fluid Mechanics,* 48**,** 285-309.

BHUNIA, A., PAIS, S. C., KAMOTANI, Y. & KIM, I. H. 1998. Bubble formation in a coflow configuration in normal and reduced gravity. *AIChE Journal,* 44**,** 1499-1509.

BROSSEAU, Q., VRIGNON, J. & BARET, J.-C. 2014. Microfluidic dynamic interfacial tensiometry (μDIT). *Soft matter,* 10**,** 3066-3076.

BRUUS, H. 2007. *Theoretical Microfluidics*, OUP Oxford.

BUZZACCARO, S., SECCHI, E. & PIAZZA, R. 2013. Ghost Particle Velocimetry: Accurate 3D Flow Visualization Using Standard Lab Equipment. *Physical Review Letters,* 111**,** 048101.

CHENG, N.-S. 2008. Formula for the viscosity of a glycerol− water mixture. *Industrial & engineering chemistry research,* 47**,** 3285-3288.

CHINAUD, M., VOULGAROPOULOS, V. & ANGELI, P. 2016. Surfactant effects on the coalescence of a drop in a Hele-Shaw cell. *Physical Review E,* 94**,** 033101.

COHEN, I. & NAGEL, S. R. 2001. Testing for scaling behavior dependence on geometrical and fluid parameters in the two fluid drop snap-off problem. *Physics of Fluids,* 13**,** 3533-3541.

CUBAUD, T. & MASON, T. G. 2008. Capillary threads and viscous droplets in square microchannels. *Physics of Fluids*.

CUI, Y., LI, Y., WANG, K., DENG, J. & LUO, G. 2020. Determination of Dynamic Interfacial Tension during the Generation of Tiny Droplets in the Liquid–Liquid Jetting Flow Regime. *Langmuir,* 36**,** 13633-13641.

DE SAINT VINCENT, M. R., PETIT, J., AYTOUNA, M., DELVILLE, J. P., BONN, D. & KELLAY, H. 2012. Dynamic interfacial tension effects in the rupture of liquid necks. *Journal of Fluid Mechanics,* 692**,** 499-510.

DIAMANT, H. & ANDELMAN, D. 1996. Kinetics of Surfactant Adsorption at Fluid− Fluid Interfaces. *The Journal of Physical Chemistry,* 100**,** 13732-13742.

DONG, T., WEHELIYE, W. H. & ANGELI, P. 2019. Laser induced fluorescence studies on the distribution of surfactants during drop/interface coalescence. *Physics of Fluids,* 31**,** 012106.

EGGERS, J. 1997. Nonlinear dynamics and breakup of free-surface flows. *Reviews of modern physics,* 69**,** 865.

EGGERS, J. & VILLERMAUX, E. 2008. Physics of liquid jets. *Reports on Progress in Physics,* 71**,** 036601.

EVERITT, B. & SKRONDAL, A. 2002. *The Cambridge dictionary of statistics*, Cambridge University Press Cambridge.

FERREIRA, J., CASTRO, F., ROCHA, F. & KUHN, S. 2018. Protein crystallization in a droplet-based microfluidic device: Hydrodynamic analysis and study of the phase behaviour. *Chemical Engineering Science,* 191**,** 232-244.

GARSTECKI, P., STONE, H. A. & WHITESIDES, G. M. 2005. Mechanism for flow-rate controlled breakup in confined geometries: A route to monodisperse emulsions. *Physical review letters,* 94**,** 164501.

GLAWDEL, T., ELBUKEN, C. & REN, C. L. 2012. Droplet formation in microfluidic T-junction generators operating in the transitional regime. I. Experimental observations. *Physical Review E,* 85**,** 016322.

GLAWDEL, T. & REN, C. L. 2012. Droplet formation in microfluidic T-junction generators operating in the transitional regime. III. Dynamic surfactant effects. *Physical Review*.

HUMPHRY, K. J., AJDARI, A., FERNÁNDEZ-NIEVES, A., STONE, H. A. & WEITZ, D. A. 2009. Suppression of instabilities in multiphase flow by geometric confinement. *Physical Review E,* 79**,** 056310.

HUSNY, J. & COOPER-WHITE, J. J. 2006. The effect of elasticity on drop creation in T-shaped microchannels. *Journal of non-newtonian fluid mechanics,* 137**,** 121-136.

KELLER, J. B. & MIKSIS, M. J. 1983. Surface tension driven flows. *SIAM Journal on Applied Mathematics,* 43**,** 268-277.

KINOSHITA, H., KANEDA, S., FUJII, T. & OSHIMA, M. 2007. Three-dimensional measurement and visualization of internal flow of a moving droplet using confocal micro-PIV. *Lab on a Chip,* 7**,** 338-346.

KORCZYK, P. M., VAN STEIJN, V., BLONSKI, S., ZAREMBA, D., BEATTIE, D. A. & GARSTECKI, P. 2019. Accounting for corner flow unifies the understanding of droplet formation in microfluidic channels. *Nature communications,* 10**,** 1-9.

KOVALCHUK, N. M., JENKINSON, H., MILLER, R. & SIMMONS, M. J. 2018a. Effect of soluble surfactants on pinch-off of moderately viscous drops and satellite size. *Journal of colloid and interface science,* 516**,** 182-191.

KOVALCHUK, N. M., NOWAK, E. & SIMMONS, M. J. 2017. Kinetics of liquid bridges and formation of satellite droplets: Difference between micellar and bi-layer forming solutions. *Colloids and Surfaces A: Physicochemical and Engineering Aspects,* 521**,** 193-203.

KOVALCHUK, N. M., NOWAK, E. & SIMMONS, M. J. H. 2016. Effect of Soluble Surfactants on the Kinetics of Thinning of Liquid Bridges during Drops Formation and on Size of Satellite Droplets. *Langmuir*.

KOVALCHUK, N. M., REICHOW, M., FROMMWEILER, T., VIGOLO, D. & SIMMONS, M. J. H. 2019. Mass Transfer Accompanying Coalescence of Surfactant-Laden and Surfactant-Free Drop in a Microfluidic Channel. *Langmuir,* 35**,** 9184-9193.

KOVALCHUK, N. M., ROUMPEA, E., NOWAK, E., CHINAUD, M., ANGELI, P. & SIMMONS, M. J. 2018b. Effect of surfactant on emulsification in microchannels. *Chemical Engineering Science,* 176**,** 139-152.

LEVICH, V. G. 1962. *Physicochemical hydrodynamics*.

MARTINO, C., VIGOLO, D., SOLVAS, X. C. I., STAVRAKIS, S. & DEMELLO, A. J. 2016. Real-Time PEGDA-Based Microgel Generation and Encapsulation in Microdroplets. *Advanced Materials Technologies,* 1**,** 1600028.

MILLS, A. J. 2016. *Investigating cetyltrimethylammonium bromide (CTAB) reverse microemulsions using nuclear magnetic resonance.* University of Birmingham.

MUCIC, N., JAVADI, A., KOVALCHUK, N. M., AKSENENKO, E. V. & MILLER, R. 2011. Dynamics of interfacial layers—Experimental feasibilities of adsorption kinetics and dilational rheology. *Advances in Colloid and Interface Science,* 168**,** 167-178.

NISISAKO, T., TORII, T. & HIGUCHI, T. 2002. Droplet formation in a microchannel network. *Lab on a Chip,* 2**,** 24-26.

NOWAK, E., XIE, Z., KOVALCHUK, N. M., MATAR, O. K. & SIMMONS, M. J. 2017. Bulk advection and interfacial flows in the binary coalescence of surfactant-laden and surfactant-free drops. *Soft Matter*.

PALA ROSAS, I., CONTRERAS, J. L., SALMONES, J., TAPIA, C., ZEIFERT, B., NAVARRETE, J., VÁZQUEZ, T. & GARCÍA, D. C. 2017. Catalytic dehydration of glycerol to acrolein over a catalyst of Pd/LaY zeolite and comparison with the chemical equilibrium. *Catalysts,* 7**,** 73.

PAPAGEORGIOU, D. T. 1995. On the breakup of viscous liquid threads. *Physics of Fluids,* 7**,** 1529-1544.

PELLEGRINO, M., SCIAMBI, A., TREUSCH, S., DURRUTHY-DURRUTHY, R., GOKHALE, K., JACOB, J., CHEN, T. X., GEIS, J. A., OLDHAM, W. & MATTHEWS, J. 2018. High-throughput single-cell DNA sequencing of acute myeloid leukemia tumors with droplet microfluidics. *Genome research,* 28**,** 1345-1352.

PERKINS, L. & GEANKOPLIS, C. 1969. Molecular diffusion in a ternary liquid system with the diffusing component dilute. *Chemical Engineering Science,* 24**,** 1035-1042.

PIRBODAGHI, T., VIGOLO, D., AKBARI, S. & DEMELLO, A. 2015. Investigating the fluid dynamics of rapid processes within microfluidic devices using bright field microscopy. *Lab on a Chip*.

QIN, N., ZHAO, P., HO, E. A., XIN, G. & REN, C. L. 2020. Microfluidic Technology for Antibacterial Resistance Study and Antibiotic Susceptibility Testing: Review and Perspective. *ACS sensors*.

RICCOMI, M., ALBERINI, F., BRUNAZZI, E. & VIGOLO, D. 2018. Ghost Particle Velocimetry as an alternative to µPIV for micro/milli-fluidic devices. *Chemical Engineering Research and Design,* 133**,** 183-194.

ROUMPEA, E., KOVALCHUK, N. M., CHINAUD, M., NOWAK, E., SIMMONS, M. J. & ANGELI, P. 2019. Experimental studies on droplet formation in a flow-focusing microchannel in the presence of surfactants. *Chemical Engineering Science,* 195**,** 507-518.

SCHNEIDER, C. A., RASBAND, W. S. & ELICEIRI, K. W. 2012. NIH Image to ImageJ: 25 years of image analysis. *Nature methods,* 9**,** 671-675.

SCHOFIELD, Z., BAKSAMAWI, H. A., CAMPOS, J., ALEXIADIS, A., NASH, G. B., BRILL, A. & VIGOLO, D. 2020. The role of valve stiffness in the insurgence of deep vein thrombosis. *Communications materials,* 1**,** 1-10.

SON, Y., MARTYS, N. S., HAGEDORN, J. G. & MIGLER, K. B. 2003. Suppression of capillary instability of a polymeric thread via parallel plate confinement. *Macromolecules,* 36**,** 5825-5833.

THORSEN, T., ROBERTS, R. W., ARNOLD, F. H. & QUAKE, S. R. 2001. Dynamic pattern formation in a vesicle-generating microfluidic device. *Phys Rev Lett,* 86**,** 4163-6.

TIMGREN, A., TRÄGÅRDH, G. & TRÄGÅRDH, C. 2008. Application of the PIV technique to measurements around and inside a forming drop in a liquid–liquid system. *Experiments in Fluids,* 44**,** 565-575.

UMBANHOWAR, P., PRASAD, V. & WEITZ, D. A. 2000. Monodisperse emulsion generation via drop break off in a coflowing stream. *Langmuir,* 16**,** 347-351.

VEN, K., VANSPAUWEN, B., PÉREZ-RUIZ, E., LEIRS, K., DECROP, D., GERSTMANS, H., SPASIC, D. & LAMMERTYN, J. 2018. Target confinement in small reaction volumes using microfluidic technologies: a smart approach for single-entity detection and analysis. *ACS sensors,* 3**,** 264-284.

WANG, K., LU, Y., XU, J. & LUO, G. 2009. Determination of dynamic interfacial tension and its effect on droplet formation in the T-shaped microdispersion process. *Langmuir,* 25**,** 2153-2158.

WU, L., LIU, X., ZHAO, Y. & CHEN, Y. 2017. Role of local geometry on droplet formation in axisymmetric microfluidics. *Chemical Engineering Science,* 163**,** 56-67.

XIA, Y. & WHITESIDES, G. M. 1998. Soft lithography. *Annual review of materials science,* 28**,** 153-184.

XU, J., DONG, P., ZHAO, H., TOSTADO, C. & LUO, G. 2012. The dynamic effects of surfactants on droplet formation in coaxial microfluidic devices. *Langmuir,* 28**,** 9250-9258.

XU, J., LI, S., LAN, W. & LUO, G. 2008. Microfluidic approach for rapid interfacial tension measurement. *Langmuir,* 24**,** 11287-11292.